# Designing Microwave Antennas for NV-Centre Magnetometry

**A Thesis**

submitted to

Indian Institute of Science Education and Research Pune
in partial fulfillment of the requirements for the
Master of Science in Quantum Technology

by

Ankit Chahar


Indian Institute of Science Education and Research Pune

April, 2026

Supervisor: Prof. Atikur Rahman

# Certificate

This is to certify that this dissertation entitled "Designing Microwave Antennas for NV-Centre Magnetometry" submitted towards the partial fulfilment of the Master of Science in Quantum Technology represents study/work carried out by Ankit Chahar from Indian Institute of Science Education and Research Pune under The supervision of Dr Prof. Atikur Rahman (IISER PUNE) during the academic year 2025–2026.

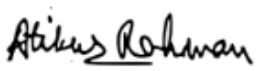

Date: 22-04-2026

**Signature of Supervisor**
(Prof. Atikur Rahman)

Date: 07-05-2026

**Signature of Advisory Member**
(Prof. Shouvik Datta)

# Declaration

I hereby declare that the matter embodied in the report entitled "Designing Microwave Antennas for NV-Centre Magnetometry" are the results of the work carried out by me at the IISER PUNE under the supervision of Prof. Atikur Rahman (IISER PUNE) and the same has not been submitted elsewhere for any other degree.

Date: April 22, 2026

Signature the Author (Ankit Chahar)

# Abstract

Nitrogen-vacancy centres in diamond are one of the most promising platforms for a wide range of applications due to their quantum sensing abilities, functionality at room temperature, and simple optical signal readout and manipulation via the use of microwave/RF radiation. Applying microwave radiation is not a very basic task depending on the application that ones want. However, in a large area within an ensemble of NV centres in a crystal or even multiple crystals, that ensemble must be addressed along with a homogeneous microwave intensity, so a more specialised microwave antenna is needed. For magnetic field sensing in NV-ensemble diamond, a wider bandwidth antenna transmission is better for sensing. For targeting this goal, a complete procedure for developing PCB-based microstrip antennas and some other very effecient PCB based antenna for NV centres applications is described in this work. For driving all NV centres that point in a given direction with the same intensity, we need uniform intensity over this area, which is not a very simple task to fabricate such an antenna [1]. At a given input power, there is always a very significant chance of compromise between a uniformness of the intensity and high intensity [2]. In this procedure of fabricating these antennas, either using feric-chloride or PCB milling in order to achieve the resolution for ODMR signal acquisition, fabrication and testing using a vector network analyser. The fabricated antennas reached a maximum transmission of 60 % (Fig. 4.3)of the input power around the desired frequency (2.87 GHz), a more than 400 MHz bandwidth (Fig. 4.3) and are well capable of resolving electronic spin resonance with a very good contrast.

# Acknowledgements

This work would not have been possible without the support and guidance of many individuals. I would like to express my sincere gratitude and thanks to:

- **Prof. Atikur Rahman** for entrusting me with this project, and for his unwavering support, insightful discussions, and constant guidance throughout this work.
- **Prof. Shouvik Datta** for his valuable advice during the course of this project and for granting access to the vector network analyser (VNA), which was essential to this work.
- **Dr H.L. Pradeep** for his generous assistance with the optical setup and for always being willing to help whenever required.
- **Himanshu** (researcher in Prof. Shouvik Datta's group) for his invaluable help with the vector network analyser and for sharing his expertise.
- **Karthikeyan S** (technical assistant, H-cross) for his continuous support and assistance during the experimental work.
- **My family and friends** for their constant encouragement, belief in me, and unwavering support throughout this journey.

I am also grateful to the entire Nano-Q lab group and the Department of Physics at IISER Pune for fostering a collaborative and stimulating research environment. I sincerely acknowledge I-Hub QTF for providing access to the necessary instruments and for their expert support, which significantly contributed to this work.

*Ankit Chahar*

# Contents

# List of Figures

# List of Tables

# Chapter 1

# Introduction

Nitrogen vacancy (NV) centres in diamonds come up as a result of a substitutional nitrogen atom (which substituted the carbon atom in the diamond lattice) and an adjacent lattice vacancy in the diamond lattice. In the last few years, this defect in diamond in its negatively charged form (NV-) has been significantly studied as a versatile spin-based quantum sensor [4](for simplicity, we just say NV centre for the negatively charged state throughout this thesis).
From the past 2-3 decades, spin-based quantum systems have become a central effort in quantum technologies. Among the many platforms explored, nuclear magnetic resonance (NMR) has played a special role. It allowed researchers to test early quantum algorithms, study decoherence, and even demonstrate counterintuitive effects. However, NMR has intrinsic limitations: at room temperature, the thermal polarisation is tiny, and one must rely on pseudo-pure states. Moreover, controlling and handling individual spins is practically impossible. These shortcomings became motivation of the researchers towards a different platform— one that can be reliable for single-spin addressability, along with maintaining the convenience of optical readout. That platform is the nitrogen-vacancy (NV) centre in the diamond. This very useful defect came in picture decades ago, this point defect has since become a leading frontier of quantum sensing and quantum information [5].

The NV centre in its negatively charged state has an electronic spin triplet (S=1) with a ground-state splitting between the ms=0 and ms=$\pm$1 levels, that energy gap is corresponding about 2.87GHz. That makes this system very attractive, because of its ability to initialise or manipulate and read out the spin state purely by optical means. A shine of green light (typically around 532nm) pumps the NV into the excited energy state, and the subsequent fluorescence intensity—stronger for ms=0 and weaker for ms = $\pm$1 — tells us the spin projection. All of this works at room temperature, under ambient conditions, and in milidiamonds.

For manipulating the spin, we need to apply resonant microwave fields. The interaction is described by the spin Hamiltonian as below

$$\frac{\hat{H}}{h} = D\,\hat{S}_z^2 + E\left(\hat{S}_x^2 - \hat{S}_y^2\right) + \gamma\,\mathbf{B}\cdot\hat{\mathbf{S}}, \tag{1.1}$$

where $D = 2.87$ GHz is the zero-field splitting,
$E$ accounts for strain,
$\gamma = g\mu_B/h$ is the gyromagnetic ratio, and
$\hat{S}_{x,y,z}$ are the $S = 1$ spin operators.

and the technique of optically detected magnetic resonance (ODMR) allows us to see the spin response via watching the fluorescence change as we sweep the microwave frequency [5]. Continuous-wave ODMR gives an efficient fingerprint of the local environment, and on the other hand, pulsed-wave ODMR can provide Rabi oscillations, Ramsey fringes, and spin echoes, allowing us to measure coherence times and implement quantum gates. The sensitivity of NVs to magnetic, electric, and thermal fields has been focused on in various applications, from nano/pico- scale magnetometry to thermometry inside living cells [6].

One of the most important parts for any ODMR experiment is a dependable microwave delivery system. The antenna or resonator must efficiently resonate a field that is strong enough, homogeneous around the sample, and when needed can work as a polarisation-controlled too. Few designs have been fabricated and tried over the years, ranging from simple wire loops to planar PCB-based stripline resonators and more fascinating tunable circuits. In particular, the ability to generate circularly polarised microwaves allows selective addressing of specific NV orientations, which is especially useful in (111)-oriented diamond samples where the centres tend to align along one axis [7].

During this work, I wanted to build a low-cost magnetometer using the ODMR phenomenon in the NV-centre overall. I also wanted to explore how significantly different antenna designs can affect the ODMR signal or the sensitivity of the signal. To this end, I built a confocal microscope from scratch, integrated it with a home-made microwave circuit, and characterized in the presence of different magnetic fields as well as in Microwave fields. This thesis describes that journey only.

## 1.1 Electron's spin manipulation using Radio Frequency

A physical system has a fundamental aspect in Quantum Mechanics where the superposition of states is different from classical states. Consider the example of a 2-level quantum system given in the following superposition state:

$$|\psi\rangle = \alpha|0\rangle + \beta|1\rangle$$

(where the norm of the coefficients must satisfy $|\alpha|^2 + |\beta|^2 = 1$). Calculate the coefficients that will give you a maximum probability. Coherence is defined by the time period during which a Superposition can continue to be maintained despite outside disturbances. This is also the maximum possible period of time that our Quantum Sensing system can be used for measuring an applied external field before losing any of the quantum information contained in the measurement.

A major contributor to decoherence in NV centres located in high-purity, low-concentration samples is the hyperfine coupling of Nuclear Spins (the surrounding Carbon-13 Nuclei) to the Electronic Spin of the NV Centre. The Carbon-13 Nuclei exist naturally within the diamond lattice at an approximate abundance of 1.1%, thus being able to generate rapidly fluctuating random nuclear spins which result in the loss of electronic spin phase memory with an always-increasing rate.

The duration of "time" it will take for the signal produced by an NV centre to decay (due to the fluctuating nuclear magnetic environments generated by other nuclear spins) is referred to as the relaxation time; this can utilise two different types of relaxation times:

- $T_1$ **(longitudinal relaxation time):** This describes how the energy stored in the electronic spin system dissipates to the surrounding environment. It is usually called the relaxation time of the spin–lattice.
- $T_2$ **(Transverse relaxation time):** This characterises the loss of phase coherence among spins in the plane which is perpendicular to the quantisation direction. It is also identified as the spin–spin relaxation time.

Although the NV centre's electronic spin can behave as a functional qubit in the absence of external magnetic flux (with the $m_s = 0$ and $m_s = \pm 1$ as a two-level quantum system). So variations in the photoluminescence intensity and in coherence times can be used to infer physical quantities such as magnetic field strength, temperature or pressure. This can be achieved by applying sequences of microwave pulses that drive the electronic spin between its ground-state sub-levels. Standard quantum sensing protocols include:

- **Rabi oscillations** – measuring the coherent population transfer between $|0\rangle$ and $|1\rangle$ as a function of RF pulse duration, which gives the Rabi frequency $\Omega$, which is dependent(proportional) to the microwave field amplitude.
- **Ramsey spectroscopy** – using a $\pi/2-\tau-\pi/2$ pulse sequence to measure free precession and extract the dephasing time $T_2^*$.
- **Spin echo (Hahn echo)** – employing a $\pi/2-\tau-\pi-\tau-\pi/2$ sequence to refocus static inhomogeneities and measure the true coherence time $T_2$.

## 1.2 Description of This Work

This Master's work is completely focused on the generation and transmission of the microwave fields for driving/manipulating the electronic spin of NV-centres in a sample (which has an ensemble of NV centres) via different designs of antennas that we have fabricated using two different methods overall:
1. PCB milling and
2. Ferric-chloride etching.

We started with a fabrication technique using a low-cost mask (CD marker) on the PCB copper surface for etching. Then we proceed with the characterisation of the antenna by physically measuring its $S_{11}$ parameter as a function of frequency using a vector network analyser, and the actual oscillating magnetic field $B_{\text{ac}}$ at the diamond location must be strong enough to drive spin transitions that we can observe for an antenna design in the simulation in the Ansys HFSS. Finally, the antenna was implemented on a milli-diamond sample doped with NV centres.

Firstly, I describe the relevant theory and physical features of NVs in the next chapter. In Chapter 3, I have introduced the functioning of antennas and their important features required for analysing their performance. In chapter 4, I have discussed for their characterisation and their performance for operating the NV-centre's electronic spin. Finally, in the last chapter, I have concluded the work and outlined the ongoing and future work that we are planning to complete in the near future, which can be done in a series of continuous efforts of building a cost-effective magnetometer based on ODMR in NVs for precision magnetic field sensing.

# Chapter 2

# Background Of The NV-Centre In Diamond

## 2.1 The Nitrogen-Vacancy Centre: Structure and Symmetry

### 2.1.1 Crystal Environment

As the name "NV-centre" itself tells us, it is a result of two defects, a Nitrogen(N) atom impurity and an adjacent vacant site instead of carbon atoms in diamond (Fig. 2.1). The nitrogen-vacancy (NV) defect is a point-type defect in the diamond.

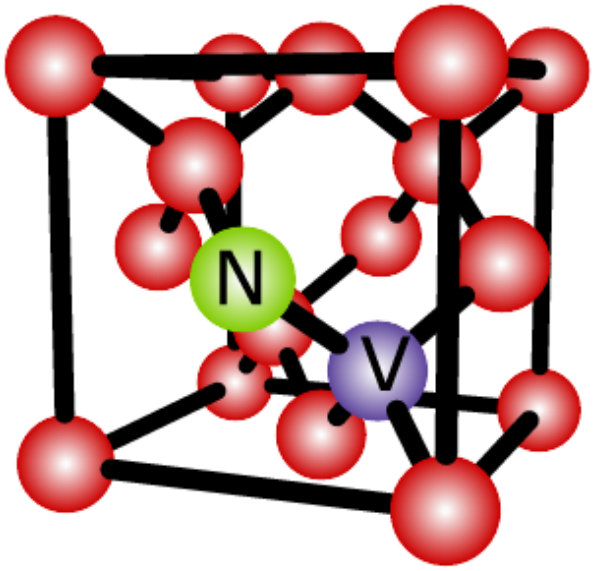


**Figure 2.1:** Representation of the presence of a single nitrogen-vacancy(NV) centre in the lattice of diamond.

The stable, negatively charged state ($NV^-$) of this defect has a total electron spin S=1 and exhibits a well-defined symmetry [8]. Because the nitrogen and the vacancy replace two adjacent carbon atoms, the defect axis is oriented along one of the four equivalent $\langle 111 \rangle$ crystallographic directions of diamond. Fig.( 2.1) illustrates this: the nitrogen-vacancy pair aligns along the line connecting the two lattice sites, which is a body diagonal of the cubic unit cell.

### 2.1.2 $C_{3v}$ Symmetry of the NV Center

Around this defect axis, the atomic arrangement is not fully cubic, and it possesses $C_{3v}$ symmetry, which means:

- **Three-fold rotational symmetry:** Rotating the structure by 120° around the NV axis makes it identical again.
- **Three vertical mirror planes:** These planes contain the NV's main axis and pass through the surrounding carbon atoms. These planes reflect the structure through any of the plane also map the defect onto itself.

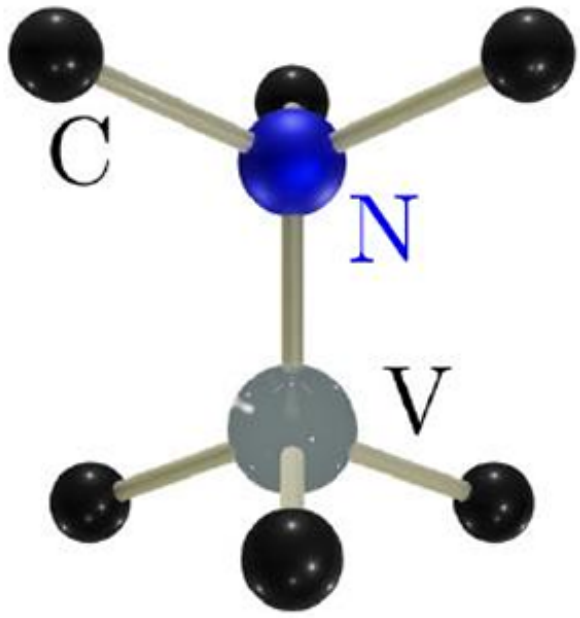


**Figure 2.2:** Structure of the NV center in a diamond showing its $C_{3v}$ symmetry.

This $C_{3v}$ point group is characteristic of a trigonal pyramid. It is lower than the full tetrahedral ($T_d$) symmetry of the perfect diamond lattice, but it is exactly what we expect for a defect-vacancy pair. This symmetry has important points for the electronic structure: it allows us to know which optical transitions are allowed and how the spin states interact with external fields [4].

### 2.1.3 Four Possible NV Orientations

Because the diamond lattice has four equivalent $\langle 111 \rangle$ directions, the NV centre can also be formed along any of these directions. In a macroscopic diamond sample, NV centres typically exist in all four orientations, unless some special growth or implantation technique is used to favour in one direction. And these four axes are conventionally labelled as:

- NV parallel to [111]
- NV parallel to $[1\bar{1}\bar{1}]$
- NV parallel to $[\bar{1}1\bar{1}]$
- NV parallel to $[\bar{1}\bar{1}1]$

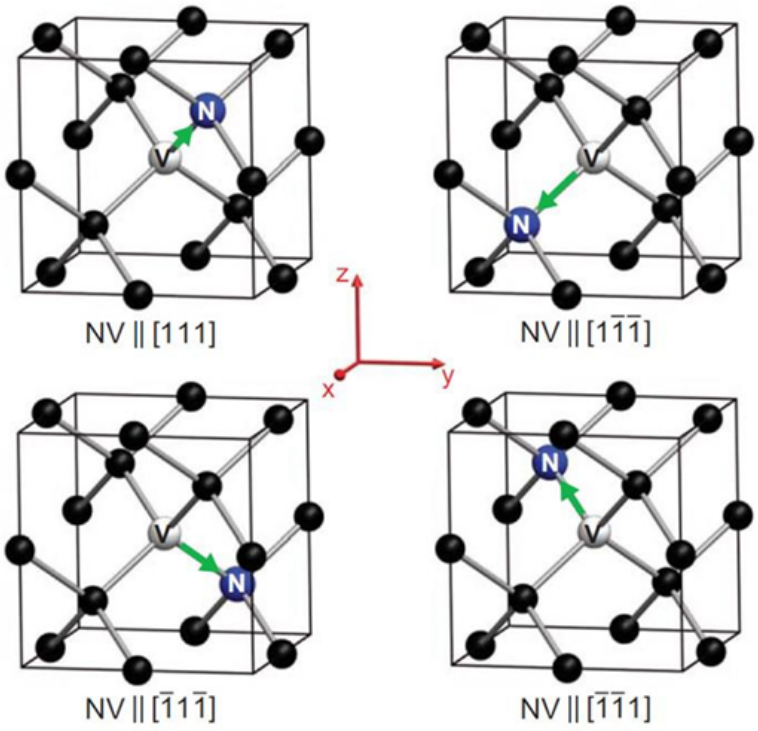


**Figure 2.3:** All four possible orientations of the NV axis in a diamond crystal, along the $\langle 111 \rangle$ directions.

Each orientation in Fig. 2.3 has its own quantisation axis. When an external magnetic field is applied, the Zeeman splitting of the $m_s = \pm 1$ levels depends on the projection of the field onto each NV axis [4, 5]. As a result, an ODMR spectrum from an ensemble containing all four orientations will show up to eight resonances (four pairs) when the magnetic field is large enough to resolve them. This multi-axis response is both a challenge (it complicates the spectrum) and an opportunity (it allows us to perform vector magnetometry).

### 2.1.4 Why Symmetry Matters in This Work

For microwave driving, the transition probability between the spin states $m_s = 0$ and $m_s = \pm 1$ is maximum and most effective when the microwave magnetic field is oriented in a perpendicular direction to the NV axis. Therefore, a single antenna can simultaneously address NV centres with different-diffrent orientations, but the effective Rabi frequency will vary according to the angle between the microwave field and each NV-axis. Designing an antenna that delivers a uniform, well-defined microwave field across the diamond is essential for quantitative measurements – and that is the central part of this master's thesis project.

## 2.2 Optical and Electronic Properties

The NV centre can exist in three different charge states: neutral ($NV^0$, spin $S = 1/2$), negative ($NV^-$, spin $S = 1$), and positive ($NV^+$, which does not fluoresce). In this work, we focus only on the negatively charged NV centre because it is the only one that gives a strong, spin-dependent fluorescence signal. From now on, when we say "NV", we mean $NV^-$ [5].

The ground state of the $NV^-$ centre is a triplet, labelled $^3A_2$. Even without any external magnetic field, the $m_s = 0$ and $m_s = \pm 1$ sublevels are not at the same energy. They are separated by about 2.87 GHz. This splitting is called the **zero-field splitting (ZFS)** (Fig. 2.4). It arises from the magnetic interaction between the two unpaired electrons (spin-spin coupling).

When we shine green light (wavelength 532nm) on the NV centre, electrons jump from the ground state to the excited state. From there, they can fall back to the ground state by emitting red light (fluorescence) in the range 630–800nm (Fig. 2.4). This red light is what we detect in our experiments (Fig. 2.5).

If we apply an external magnetic field along the NV axis, the Zeeman effect lifts the degeneracy of the $m_s = \pm 1$ levels. They split apart linearly with the field strength. The splitting is given by:

$$\Delta f = 2\gamma_e B_{\parallel}$$

where $\gamma_e = 2.8$ MHz/G is the electron gyromagnetic ratio and $B_{\parallel}$ is the magnetic field component parallel to the NV axis. This is the key phenomenon for magnetic field sensing.

The so-called **zero-phonon line (ZPL)** is a sharp peak in the emission spectrum. For $NV^-$ it lies at 637nm; for $NV^0$ it is at 575nm. By examining the ZPL, we can determine which charge state is present in our diamond sample [5].

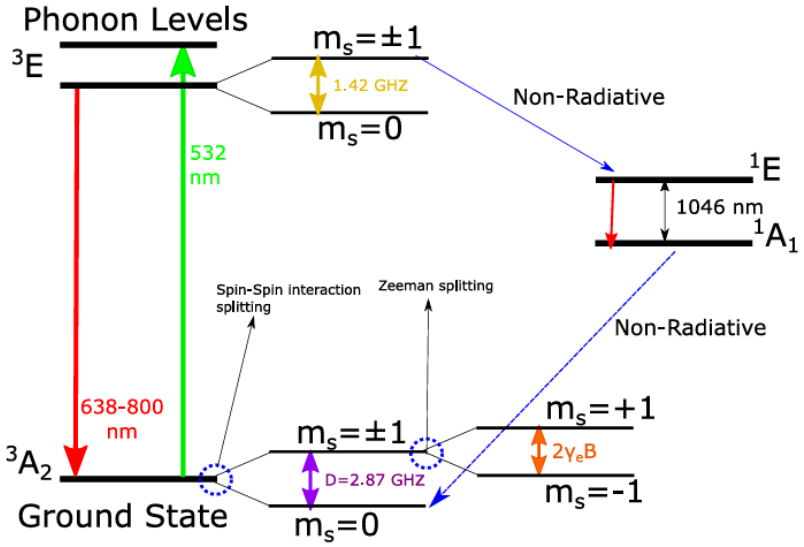


**(a)** Complete energy level diagram of the $NV^-$ centre showing the ground state $^3A_2$, excited state $^3E$, and the intermediate singlet states $^1A_1$ and $^1E$. The green arrow indicates optical excitation (532nm), the red arrow shows fluorescence (637nm zero-phonon line), and the side arrows represent non-radiative intersystem crossing.

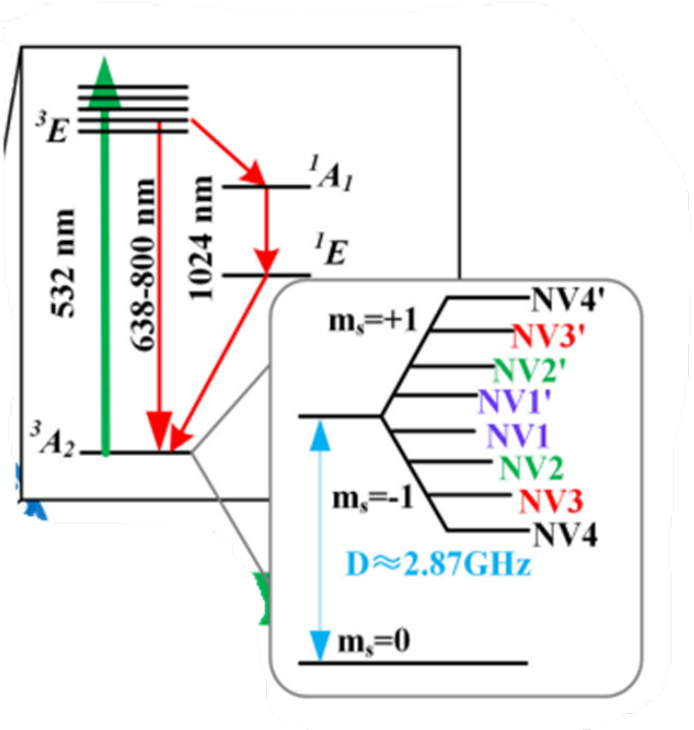


**(b)** Simplified energy level diagram focusing on the triplet states while all 4 orientations of the NVs are present. The zero-field splitting $D = 2.87$ GHz separates $m_s = 0$ from $m_s = \pm 1$. The infrared transition at 1024nm between the singlet states is also shown.

**Figure 2.4:** Energy level structure of the negatively charged nitrogen-vacancy centre. (a) Complete diagram including singlet states. (b) Simplified diagram highlighting the triplet states and the zero-field splitting.

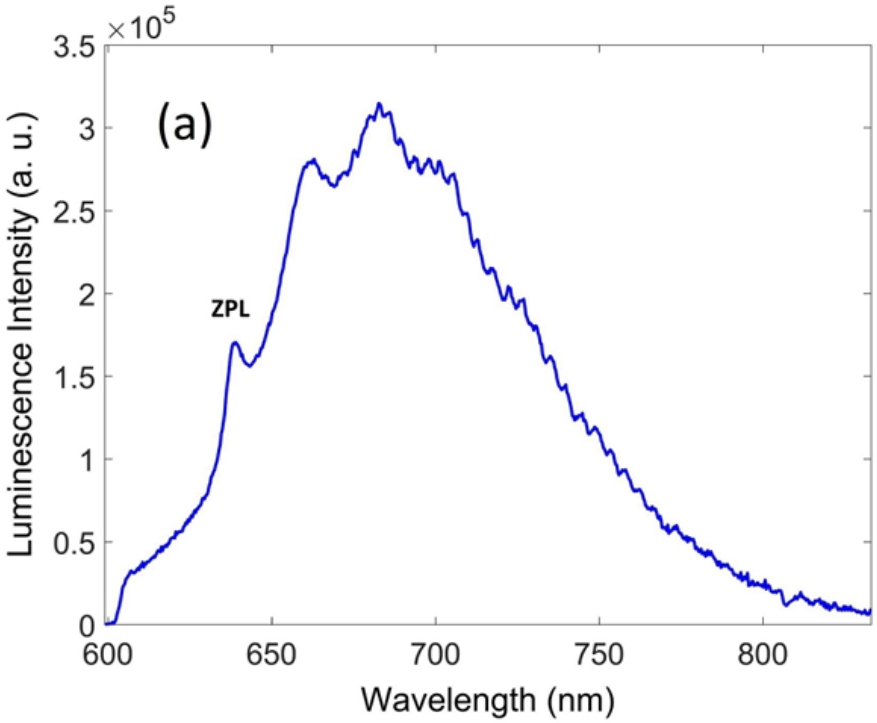


**Figure 2.5:** Emission spectrum of NV centres in diamond. The zero-phonon lines (ZPL) of $NV^0$ and $NV^-$ are at 575 nm and 637 nm, respectively. The broad vibronic sidebands are due to phonon-assisted transitions. The ZPL positions allow unambiguous identification of the charge state.

## 2.3 Spin Properties and Optical Polarisation

One of the very useful properties of the NV centre is that its spin state can be prepared and manipulated, and its state can be read out at room temperature [9].

### 2.3.1 Polarizing the spin into $m_s$=0

When we regularly shine a green laser on the NV centre, after a few excitation–decay cycles, the electron spin ends up almost always in the $m_s$=0 ground state. This happens due to the following reasons:

- From the excited state, the decay back to $m_s = 0$ is very fast (about 10 ns) and produces bright fluorescence.
- If the electron happens to be in $m_s = \pm 1$, it takes a different path: it goes through a dark, metastable state ($^1A_1$) that has a much longer lifetime (about 300 ns) [10]. During that time, it does not emit fluorescence, and eventually it falls back to $m_s = 0$.

So, after a short time, almost all NV centres are "pumped" into the bright $m_s = 0$ state. This process is called **optical pumping**.

### 2.3.2 Why the Fluorescence Depends on Spin

Because the $m_s = \pm 1$ states spend time in the dark metastable state, and these excitations decay via the intersystem crossing; So, their overall fluorescence is much weaker than that of $m_s$=0. These decay emissions are not in the visible range, which is why we call them dark transitions, and these states are called as "Dark state" [**?** ]. At the end, this difference in brightness is what allows us to “read out” the spin state by simply measuring the intensity of the red light.

## 2.4 Interaction Hamiltonian (Brief Overview)

For completeness, we give the Hamiltonian that describes the NV centre's spin interactions. It has three components overall:

- $H_S$: the electronic spin part, including the zero-field splitting and the Zeeman term.
- $H_I$: the nuclear spin part (the nitrogen nucleus, mostly $^{14}$N, has spin $I = 1$).
- $H_{S-I}$: the hyperfine coupling between the electron and the nitrogen nucleus.

The full Hamiltonian is:

$$H = H_S + H_I + H_{S-I} \tag{2.1}$$

with

$$H_S = DS_z^2 + E(S_x^2 - S_y^2) + \gamma_e \, \vec{B} \cdot \vec{S} \tag{2.2}$$

$$H_I = PI_z^2 - \gamma_n \, \vec{I} \cdot \vec{B} \tag{2.3}$$

$$H_{S-I} = A_{\parallel} S_z I_z + A_{\perp}(S_x I_x + S_y I_y) \tag{2.4}$$

Here $D = 2.87\,\mathrm{GHz}$ is the zero-field splitting, $\gamma_e = 2.8\,\mathrm{MHz/G}$ is the electron gyromagnetic ratio, $\gamma_n = 1.07\,\mathrm{kHz/G}$ is the nuclear gyromagnetic ratio, and $A_{\parallel}$, $A_{\perp}$ are hyperfine constants. For most of this thesis work, we do not need the full Hamiltonian; we only need to know that a microwave field perpendicular to the NV axis can drive transitions between $m_s = 0$ and $m_s = \pm 1$.

## 2.5 Optical Readout with Confocal Microscopy

For detecting the weak fluorescence from NV centres, we need to separate this out from the strong green excitation light. A common way to use a confocal microscope is shown in (Fig. 2.6). Here is how it works:

- A green laser beam is reflected by a dichroic mirror (a mirror/filter that reflects green but transmits red) and focused onto the diamond sample. Simply, we can just use a red filter too, for the same purpose.
- The sample emits red fluorescence. This red light travels back along the same path as the incident light, but now it passes through the dichroic mirror instead of being reflected; it is transmitted.
- Before reaching to the detector, ideally, we should pass the light through a pinhole. The pinhole blocks light that comes from out-of-focus planes. Only light from a tiny, diffraction-limited spot reaches the detector. This detection (including the pinholes in the setup) technique is able to give very good spatial resolution.

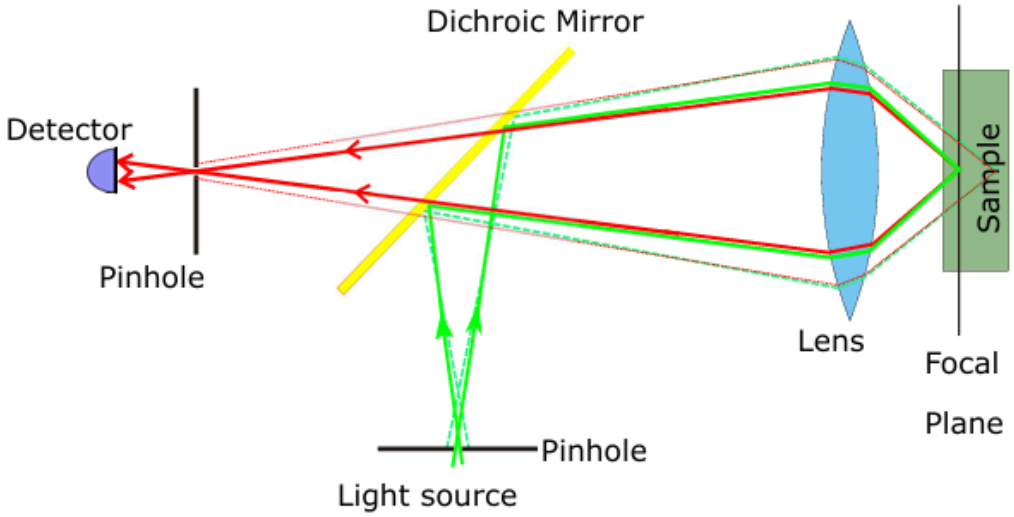


**Figure 2.6:** Schematic of the optical setup using a dichroic mirror, lens, pinhole, and detector for sample imaging.

In our work, we use a simpler setup (no pinhole, just a lens and a photodiode) because we are interested in large areas, not single NV centres. But the basic principle of using a dichroic mirror and a filter remains the same.

## 2.6 Optically Detected Magnetic Resonance (ODMR)

ODMR is the main tool we use to detect when the microwave field is resonant with the NV spin transition [11]. The procedure for that is as simple as follows (Fig. 2.7):

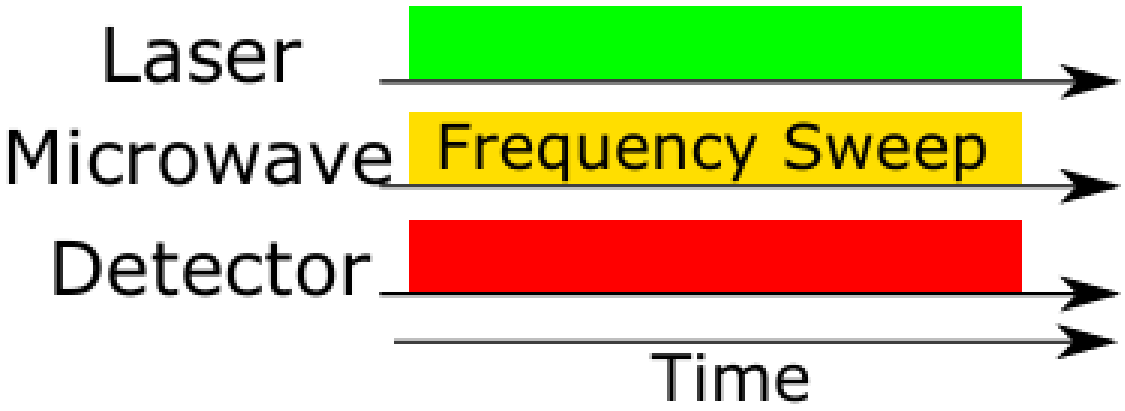


**Figure 2.7: ODMR pulse sequence.** The green excitation continuously polarises the NV centre to its ground state, while the microwave frequency is swept and the detector is always on.

1. We shine a continuous green light on the diamond. This polarises the NV centres into the bright/excited $m_s = 0$ state. The fluorescence of these transitions is high.

2. At the same time, when we sweep the frequency of a microwave signal applied to the antenna.

3. When the microwave frequency matches the $m_s = 0 \leftrightarrow m_s = \pm 1$ transition, some of the population is transferred to the dark $m_s = \pm 1$ states, and the fluorescence get drops.

4. By recording the fluorescence intensity as a function of microwave frequency, we obtain a spectrum with dips at the resonance frequencies.

If no external magnetic field is present, the dip is centred at $f_0 = 2.87\,\text{GHz}$. The shape of the dip is well described by a Lorentzian function:

$$I(f) = I_0 - \frac{C}{1 + \left(\frac{f - f_0}{\Gamma}\right)^2} + D(f - f_1) \tag{2.5}$$

Here:

- $I_0$ is the average fluorescence away from resonance in the absence of a magnetic field.

- $C$ is the contrast (depth of the dip).
- $\Gamma$ is the half-width at half-maximum, related to the full width at half maximum (FWHM $= 2\Gamma$).
- The last term $D(f - f_1)$ accounts for any slow drift in the signal.

When we bring a permanent magnet close to the diamond, the magnetic field splits the $m_s = \pm 1$ levels. The single dip becomes **two dips** — one for the $m_s = 0 \rightarrow +1$ transition and one for $m_s = 0 \rightarrow -1$. The splitting between the two dips is $\Delta f = 2\gamma_e B_{\parallel}$. By measuring $\Delta f$, we can calculate the magnetic field. This is the principle of an NV magnetometer (Figure 2.8).

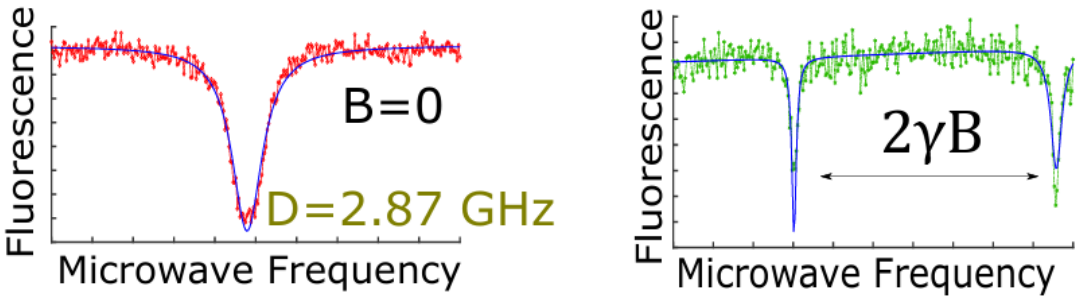


**Figure 2.8: ODMR spectrum** [3]. Without a magnetic field, the spectrum looks like the left side of the figure. If there is a magnetic field applied, the spectrum looks like the right side figure, with the splitting between the two peaks proportional to the applied field intensity along the NV axis.

If more than one NV orientation is present (which is a typical thing), and the magnetic field is not perfectly aligned with one axis and the field is strong enough, we may see up to four pairs (different electronic sub-levels, Fig. 2.4) of dips (eight dips total), Fig. 2.9 [12]. In this thesis, we work with polycrystalline diamonds where all orientations are present [5].

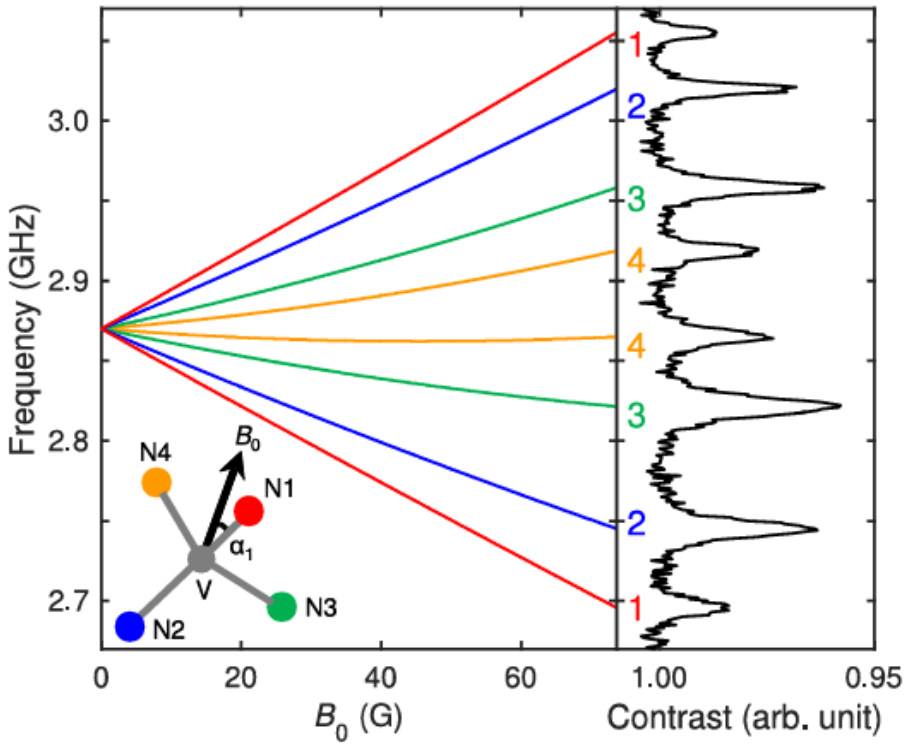


**Figure 2.9:** CW ODMR spectrum and magnetic-field-dependent transition frequencies for four NV orientations. Eight resonances are observed at $B_0 = 74$ G due to Zeeman splitting [3].

## 2.7 Manipulating the Ground State with Microwave Pulses

So far, we have described **continuous-wave (CW) ODMR**, where the microwave is always ON while we sweep the frequency. We can also use short microwave **pulses** to perform more advanced experiments, such as measuring how long the spin can stay in a superposition (coherence time).

### 2.7.1 Rabi Oscillations

When we tune the microwave frequency exactly to the resonance (e.g., 2.87 GHz). Then we apply a microwave pulse for a certain duration $t$ and measure the fluorescence afterwards. Initially (pulse duration zero), the spin is in $m_s = 0$, and the detected fluorescence is high. As the pulse gets longer, the spin rotates away from $m_s = 0$ toward a superposition of $m_s = 0$ and $m_s = \pm 1$ (Figure 2.10). The fluorescence drops. If the pulse is just the right length, we can put the spin completely into the dark $m_s = \pm 1$ state – this is called a $\pi$ pulse. If we continue increasing the pulse

length, the spin rotates back to $m_s = 0$, and the fluorescence returns to its maximum. This back-and-forth oscillation is called a **Rabi oscillation** [13].

The frequency of the Rabi oscillation, $\Omega$, is directly dependent on the strength of the microwave magnetic field. By measuring $\Omega$, we can characterise how well our antenna delivers microwave power to the NV centres. The probability of finding the spin in the $m_s = 1$ state (dark) as a function of time is approximately:

$$P(t) = \frac{\Omega^2}{\Omega_{\text{eff}}^2} \sin^2(\Omega_{\text{eff}} t) \tag{2.6}$$

where

$$\Omega_{\text{eff}} = \sqrt{\delta^2 + \Omega^2} \tag{2.7}$$

and $\delta$ is the detuning (how far the microwave frequency is from the exact resonance).

In real experiments, the oscillations decay over time because of environmental noise. A more realistic fit includes an exponential decay:

$$f(t) = A\left[1 - B\cos(\Omega t + \phi)\right] e^{-t/T_1} + C \tag{2.8}$$

Here, $T_1$ is the longitudinal relaxation time (energy relaxation), not to be confused with the dephasing time.

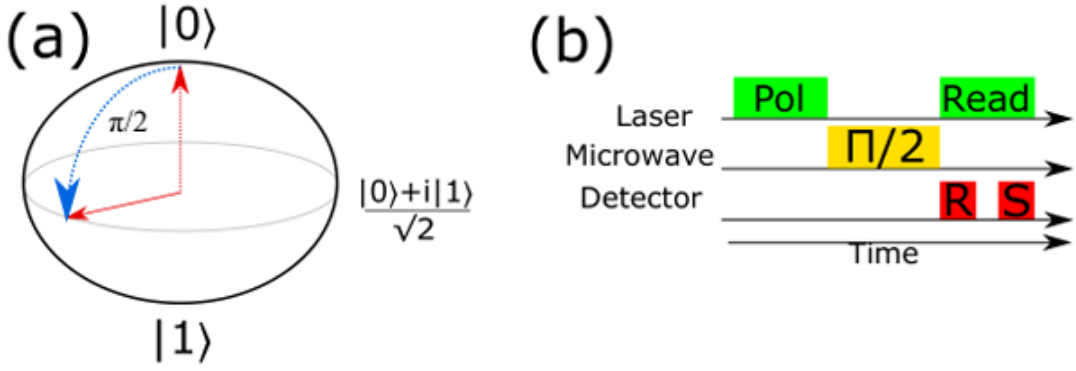


**Figure 2.10:** Ground-state manipulation via Rabi oscillations. (a) A two-level system is driven by a $\pi/2$ microwave pulse, which rotates the state from $|0\rangle$ to a coherent superposition on the equatorial plane of the Bloch sphere. For a $\pi/2$ rotation about the $x$-axis, the resulting state is $|\psi\rangle = \frac{1}{\sqrt{2}}(|0\rangle + i\,|1\rangle)$. (b) Experimental pulse sequence: an initial green laser pulse initialises (polarises) the NV centre into the $|0\rangle$ state, followed by a microwave pulse that generates and manipulates the superposition. A subsequent laser pulse performs the readout. The fluorescence is first recorded as a reference signal and then measured again to determine the population in the $|0\rangle$ ($m_s = 0$) state.

### 2.7.2 Ramsey Spectroscopy

Rabi oscillations tell us how well we can **drive** the spin. To measure how long the spin can **remember** a superposition state (coherence time $T_2^*$), we use a Ramsey sequence [14]. The sequence is:

- A $\pi/2$ pulse rotates the spin from $m_s = 0$ to an equal superposition $(|0\rangle + |1\rangle)/\sqrt{2}$.
- We wait for a time $\tau$. During this wait, the spin precesses freely under the influence of any background magnetic field.
- A second $\pi/2$ pulse is applied. Depending on how much the spin has precessed, the final fluorescence will vary.
- By repeating the experiment for different $\tau$, we get an oscillating signal that decays with a time constant $T_2^*$ – the **spin dephasing time**.

The signal is given by:

$$p(t) = \frac{1}{2}\left(1 - e^{-(t/T_2^*)^2} \sum_{j=1}^{N} a_j \cos(\Omega_j t + \phi_j)\right) \tag{2.9}$$

In this thesis we focus mainly on CW-ODMR and Zeeman splitting. Rabi and Ramsey measurements are left for future work, but the theoretical background is included here for completeness.

# Chapter 3

# Microwave Antennas for NV Centre Spin Manipulation

## 3.1 Fundamentals of Microwave Antennas

An antenna is a device that converts electrical signals into electromagnetic waves (and vice versa). In the context of NV-centre experiments, the antenna generates an oscillating/microwave magnetic field $B_{ac}$ that drives transitions between the $m_s = 0$ and $m_s = \pm 1$ spin sub-levels [14, 15]. The performance of an antenna is characterised by the following three interrelated properties [16]:
1.impedance,
2.spectral response and
3.spatial field distribution

### 3.1.1 Impedance and Reflection Coefficient

The antenna presents a load impedance $Z_L = R + iX$ to the microwave source [14]. For maximum power transfer, the source impedance $Z_0$ (typically $50\,\Omega$) must be matched to $Z_L$. The degree of mismatch is quantified by the voltage reflection coefficient $\Gamma$:

$$\Gamma = \frac{Z_L - Z_0}{Z_L + Z_0} \tag{3.1}$$

The return loss $S_{11}$ (in dB) is given by

$$S_{11} = 20 \log_{10} |\Gamma|. \tag{3.2}$$

A value of $S_{11} \leq -10\,\mathrm{dB}$ is generally considered acceptable, indicating that at least 90% of the incident power is delivered to the antenna.

### 3.1.2 Spectral Properties

One of the important characteristics for the NV-magnetometry of an antenna is how the radiated power is distributed among frequencies [2]. The antenna's frequency response is described by its resonance frequency $f_r$ and bandwidth $\Delta f$. For NV centres, the zero-field splitting is $D = 2.87\,\text{GHz}$, so the antenna should ideally resonate at this frequency. The bandwidth determines how far the resonance can be shifted by an external magnetic field (via Zeeman splitting) without losing efficiency. A wider bandwidth also relaxes fabrication tolerances and environmental sensitivity. The quality factor $Q = \frac{f_r}{\Delta f}$ relates the sharpness of the resonance to energy storage versus loss [15].

### 3.1.3 Spatial Field Uniformalty

The distribution pattern of the power which is radiated over the 3D-space is known as **radiation-pattern**. For ensemble NV magnetometry, a uniform microwave magnetic field over the diamond area is crucial. Inhomogeneous $B_{\text{ac}}$ leads to position-dependent Rabi frequencies, which broaden the ODMR line and reduce sensitivity [**?** **?** ]. The ideal antenna produces a constant $B_{\text{ac}}$ amplitude over the sample volume, with the field direction perpendicular to the NV axis for maximum transition probability '[17].

## 3.2 Microstrip Patch Antennas – A Simple Starting Point

Microstrip antennas consist of a metallic patch on a dielectric substrate with a ground plane on the opposite side. They are planar, lightweight, and compatible with standard PCB fabrication(Figure 3.1). The resonance frequency of a rectangular patch is approximately [18]:

$$f_r \approx \frac{c}{2L\sqrt{\varepsilon_{\text{eff}}}} \tag{3.3}$$

where $L$ is the patch length and $\varepsilon_{\text{eff}}$ is the effective permittivity of the substrate(FR4). The characteristic impedance of the feeding line is given by the Wheeler equations [18]. For a microstrip line of width $W$ and substrate height $H$, the effective permittivity is:

$$\varepsilon_{\text{eff}} = \frac{\varepsilon_r + 1}{2} + \frac{\varepsilon_r - 1}{2\sqrt{1 + 12H/W}} \tag{3.4}$$

and the impedance is:

$$Z_0 = \begin{cases} \frac{60}{\sqrt{\varepsilon_{\text{eff}}}} \ln\left(\frac{8H}{W} + \frac{W}{4H}\right), & \text{for } \frac{W}{H} \leq 1 \\ \frac{120\pi}{\sqrt{\varepsilon_{\text{eff}}}\left(\frac{W}{H} + 1.393 + 0.667 \ln\left(\frac{W}{H} + 1.444\right)\right)}, & \text{for } \frac{W}{H} > 1 \end{cases} \tag{3.5}$$

These equations allow the design of a $50\,\Omega$ feed line for a given substrate (For example, we have used FR-4, $\varepsilon_r \approx 4.3$, $H = 1.6\,\text{mm}$).

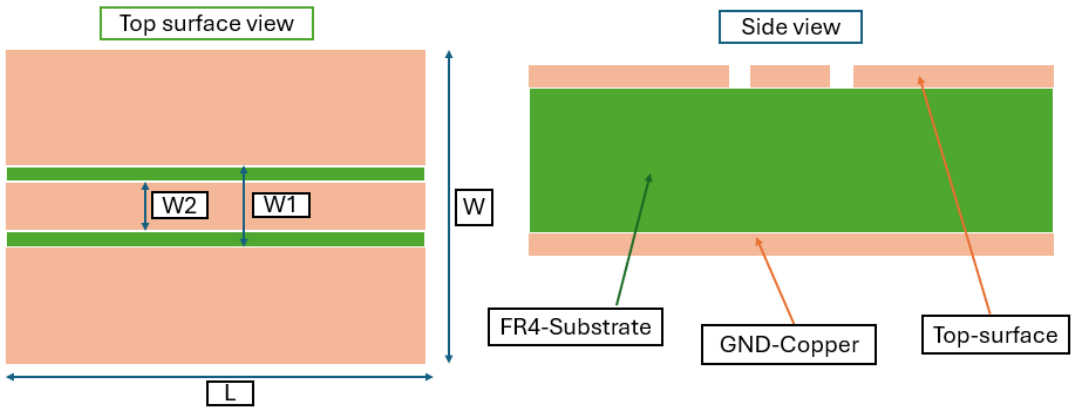


**Figure 3.1:** Full design with all necessary parameters for the microstrip patch antenna (all dimensions are based on simulations performed in the ANSYS HFSS tool). The geometrical and material parameters of the microstrip structure are summarised in Table 3.1.

**Table 3.1:** Geometrical parameters of the microstrip structure (top and side view)

| **Parameter** | **Description** | **Value (mm)** |
|---|---|---|
| $L$ | Substrate length | 26 mm |
| $W$ | Substrate width | 25 mm |
| $W_1$ | total width of microstrip including outer gaps | 5 mm |
| $W_2$ | Width of the centeral microstrip | 3 mm |
| | *Material and Layer Properties* | |
| $h_s$ | Substrate thickness (FR-4) | 1.6 mm |
| $t_c$ | Copper thickness (top layer) | 35 $\mu$m |
| $t_g$ | Ground plane thickness | 35 $\mu$m |
| $\epsilon_r$ | Relative permittivity of substrate | 4.3 |
| $\tan\delta$ | Loss tangent of substrate | 0.02 |

I have fabricated a total of three antennas overall of this design using the ferric-chloride etching method to see the variation behaviour of this design and target a better bandwidth and higher power transmission of the antenna. So, the variations and the result are described in the next chapter.

## 3.3 Design and Fabrication of the Rectangular Spiral Coplanar RF Antenna

After exploring different microwave antenna geometries, we selected a rectangular spiral coplanar antenna for our work. This design provides a good balance between compact size, ease of fabrication, and efficient microwave delivery [16]. Compared to simple loop antennas, the spiral geometry increases the effective electrical length, allowing us to achieve resonance near the NV centre frequency (2.87 GHz) without increasing the overall footprint.

### 3.3.1 Geometry and Materials

Figure 3.2 shows the layout of the fabricated antenna. The structure is implemented on a standard FR-4 substrate based single-side copper cladded PCB-board with a relative permittivity $\epsilon_r \approx 4.3$ and thickness of 1.6 mm. Copper layers of thickness $\sim 35\,\mu$m are present on a single side: the patterned antenna is on the top surface.

The antenna consists of a rectangular spiral trace surrounded by a ground region on the same plane. The spiral geometry allows the current to travel a longer path, effectively increasing inductance while maintaining a compact design.

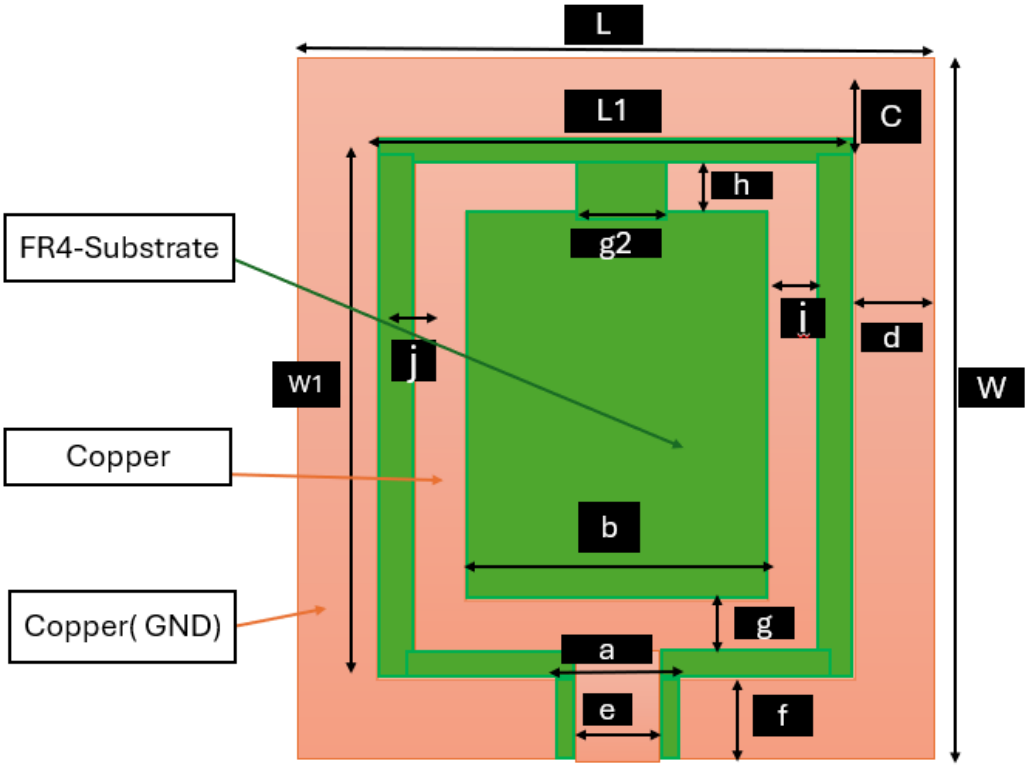


**Figure 3.2:** Short Loop antenna for microwave transition, fabricated using PCB etching method via creating a mask using the CD-marker

The key geometrical parameters (as indicated in the figure 3.2) are:

- Substrate dimensions ($L \times W$)
- Outer spiral length ($L_1$) and width ($W_1$)
- Conductor width ($c$)
- Spacing between adjacent turns ($g_2$)
- Inner region size ($b$)
- Bottom segment length ($a$)
- Gap between spiral and ground ($d$)
- Split gap at the top ($h$)
- Feedline width ($e$)
- Inner arm widths ($i, j$)

All geometrical and material parameters of the structure are summarised in Table 3.2. Similarly, as the above design, I have tried several antennas of this design too, varying the parameters a bit in a series of trying to get a better bandwidth, high power transmission and low power reflection [19]. Those variations and their results are explained later in the next chapter.

The feedline is directly connected to the spiral trace and is designed to provide impedance matching with a standard 50 Ω RF source. An SMA connector is soldered between the feedline(inner-rectangular feed, which is connected to the inner spiral loop ) and the outer loop(the bigger loop, ($L \times W$)) as ground with two outer legs of the SMA-connector for signal input, as shown in the Figure 3.3.

### 3.3.2 Working Principle

When a microwave signal is applied to the antenna, current flows along the spiral path and the surrounding ground plane. Due to the spiral geometry, the structure behaves like an effective inductive element, while the gaps between the spiral turns and the split at the top introduce capacitance [2].

Together, these effects form an equivalent LC resonator. At resonance (designed close to 2.87 GHz), the electromagnetic field is strongly confined within the gaps of the spiral structure.

The magnetic field generated by the antenna is primarily localised near the inner region and between adjacent turns of the spiral [20]. This is the region where

the diamond sample is placed during ODMR experiments. Since the magnetic field lies mostly in the plane of the substrate, the sample orientation can be adjusted to maximise interaction with the NV centres.

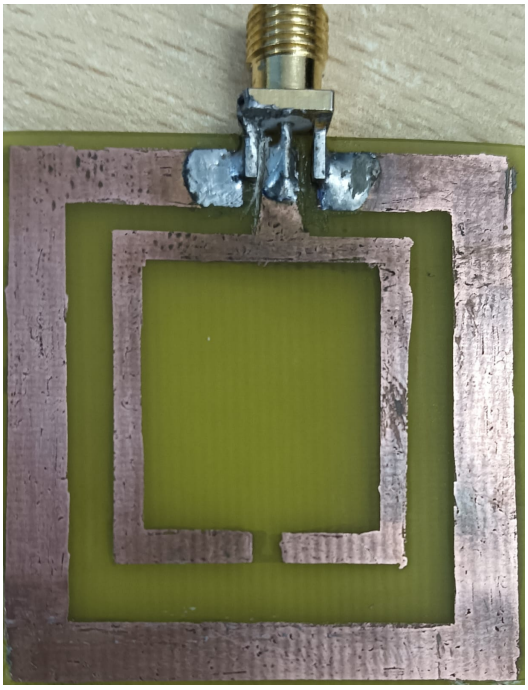

**Figure 3.3:** Fabricated real antenna showing the exact connections

### 3.3.3 Why This Design Is Useful

- **Compact and efficient:** The spiral structure increases the electrical length, allowing resonance at microwave frequencies without requiring a large physical size.
- **Strong and localised field:** The magnetic field is concentrated within the spiral gaps as well as the centre of the design, providing efficient coupling to the NV centres.
- **Easy fabrication:** The antenna can be fabricated using standard PCB techniques such as chemical etching or milling.
- **Cost-effective:** FR-4 substrate and copper layers make the design inexpensive and accessible.
- **Compatible with ODMR setup:** The planar geometry allows easy placement of the diamond sample and optical access from the top.

**Table 3.2:** Geometrical parameters of the proposed rectangular spiral RF antenna

| Parameter | Description | Value |
|---|---|---|
| | *Substrate Dimensions* | |
| $L$ | Substrate length | 38 mm |
| $W$ | Substrate width | 40 mm |
| | *Outer Loop Geometry* | |
| $L_1$ | Outer loop horizontal length | 29 mm |
| $W_1$ | Outer loop vertical length | 32 mm |
| $c = f$ | Outer conductor loop width | 4 mm |
| $d$ | outer loop width in horizontal sides | 4.5 mm |
| | *Inner Spiral Geometry* | |
| $a$ | Bottom inner segment length | 4 mm |
| $b$ | Inner square side length | 20 mm |
| $g$ | width of the conductor Bottom side of inner loop | 3 mm |
| $g_2$ | Top spacing between turns | 3 mm |
| $h$ | | |
| $i = j$ | Inner loop's conductor width (right/left vertical arm) | 3 mm |
| | *Feed Line Parameters* | |
| $e$ | Feedline width | 3 mm |
| – | Feedline length | 6 mm |
| | *Materials* | |
| — | Substrate material (FR-4) | $\epsilon_r \approx 4.3$ |
| — | Conductor material (Copper) | Thickness: 35 $\mu$m |

### 3.3.4 Fabrication Procedure

The antenna was fabricated using a standard ferric chloride ($FeCl_3$) etching process:

1. A single-sided copper-clad FR-4 board was cleaned using acetone and isopropanol.

2. A positive photo-resist was spin-coated on the top copper layer. I have drawn a mask for using the ferric-chloride etching. Even a mask drawn with a CD marker is good enough with a low-concentration ferric-chloride solution.

3. The antenna pattern (designed in CAD software) was printed on a transparency mask and aligned on the substrate. And via CD marker, we have drawn the pattern using a pen-plotter for precision.

4. The board was exposed to UV light to transfer the pattern. Via another method, we don't need this step.

5. The exposed photoresist was developed, leaving the desired copper regions protected.

6. The board was etched in heated $FeCl_3$ solution to remove unwanted copper.

7. The remaining photoresist was removed later, and the board was rinsed with deionised water.

8. Finally, an SMA edge connector was soldered between the feedline and ground, Figure 3.3.

For rapid prototyping, the same design can also be fabricated using a PCB milling machine, which avoids chemical processing and significantly reduces fabrication time. Here I am describing the whole procedure for this etching process via the help of an illustration with real images in my process.

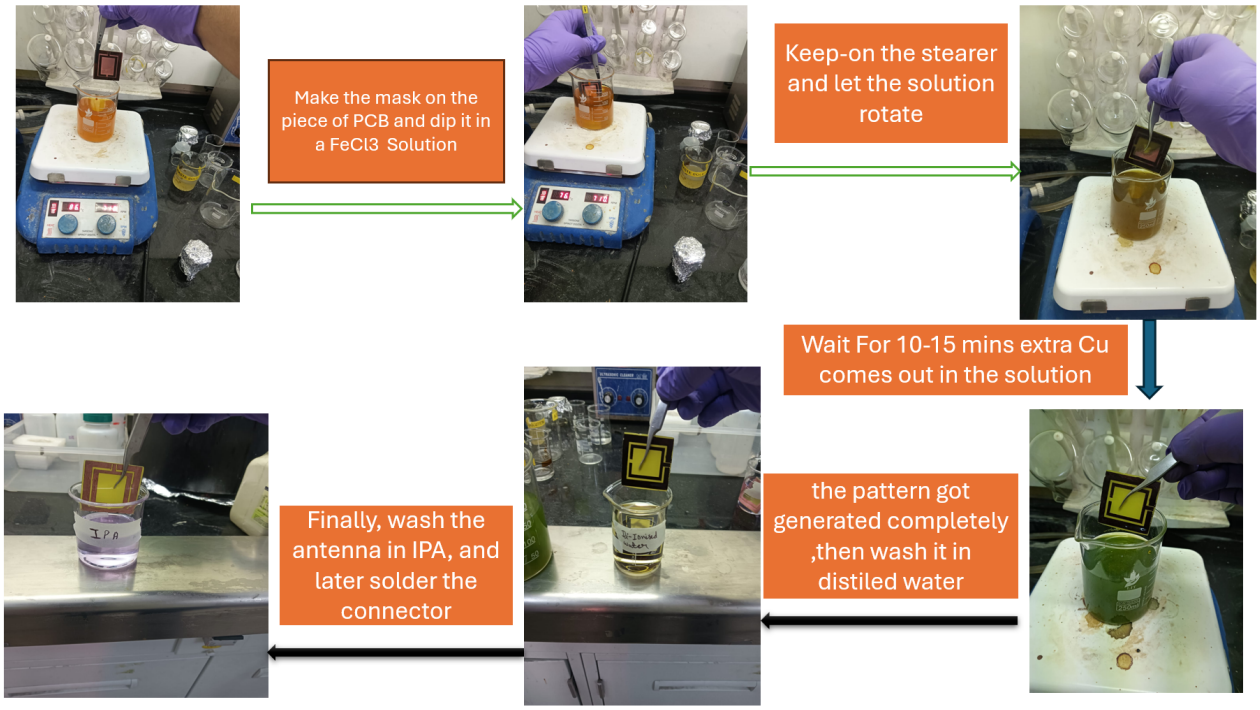


**Figure 3.4:** The complete procedure for the PCB etching using ferric-chloride solution

### 3.3.5 Summary

In summary, the rectangular spiral coplanar antenna provides a simple and effective solution for delivering microwave signals in NV-based ODMR experiments. Its all features like–compact geometry, efficient field confinement, and easy to fabricate, make it well-suited for both laboratory setups and portable sensing applications.

## 3.4 Microstrip Annular Slot Antenna

To complement the coplanar spiral antenna, we have also designed a microstrip annular slot antenna. This design is compact, easy to fabricate, and provides reliable performance near the NV centre resonance frequency of 2.87 GHz [21]. It is especially useful when stable impedance matching and moderate bandwidth are required.

### 3.4.1 Geometry and Materials

The layout of the antenna is shown in Fig. 3.5. The structure is fabricated on a Rogers (RO4350B) substrate with a relative permittivity $\epsilon_r \approx 3.48$ and a thickness of 1.52 mm.

The bottom surface is $0.5mm \times 14.2mm$ area covered with copper and acts as a ground plane, while the top surface contains the patterned copper trace forming the antenna.

The antenna consists of three main parts:

- A straight microstrip feedline
- A circular annular loop
- A short tuning stub connected near the loop

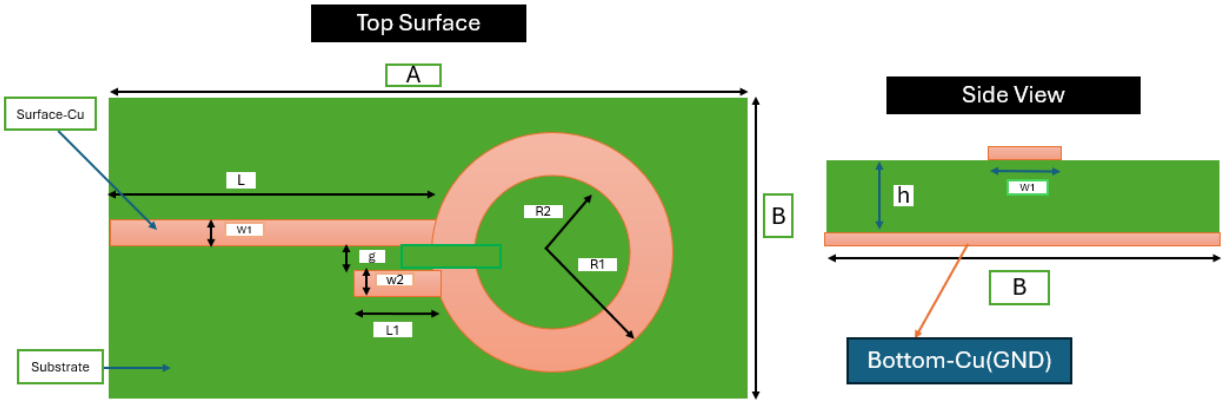


**Figure 3.5:** Design of the Circular antenna showing all the parameters

The substrate has overall dimensions $A \times B$, as indicated in the top view. The feedline of length $L$ and width $W_1$ is designed to provide approximately 50 Ω impedance for efficient power transfer.

The main radiating element is the annular loop. It is defined by an outer radius $R_1$ and an inner radius $R_2$, forming a ring-shaped current path. This loop is not directly closed; instead, it is excited through a small gap $g$ between the feedline and the loop.

A short rectangular stub of width $W_2$ and length $L_1$ is attached near the feeding region. This stub plays an important role in tuning the antenna response.

All the relevant geometrical and material parameters are listed in Table 3.3.

**Table 3.3:** Geometrical and material parameters of the microstrip annular slot antenna

| **Parameter** | **Description** | **Value (mm)** |
|---|---|---|
| | *Substrate Dimensions* | |
| $A$ | length of the substrate (top surface) | 34 mm |
| $B$ | width of the substrate | 14.2 mm |
| | *Feedline Geometry* | |
| $L$ | Feedline length | 18 mm |
| $W_1$ | Feedline width | 0.6 mm |
| | *Annular Slot (Loop)* | |
| $R_1$ | Outer radius of the loop | 3.5 mm |
| $R_2$ | Inner radius of the loop | 2 mm |
| | *Gap and Stub* | |
| $g$ | distance between feedline and the tuning strip (stub) | 0.5 mm |
| $W_2$ | Stub width | 0.6 mm |
| $L_1$ | Stub length | 3.2 mm |
| | *Material Properties* | |
| – | Substrate (Rogers RO4350B) permittivity | $\epsilon_r \approx 3.48$ |
| – | Substrate thickness | 1.52 mm |
| – | Copper thickness | 35 $\mu$m |

### 3.4.2 Working Principle

When a microwave signal is sent in the feedline via the SMA connector, as shown in Figure 3.6, it couples into the annular loop through the small gap $g$. This coupling generates a capacitance effect, while the circular current flowing around the loop behaves as inductance.

Together, these two effects create a resonant structure functioning as an LC circuit. At the resonance frequency (close to 2.87 GHz), the antenna becomes well matched to the input impedance, and most of the microwave power is efficiently transferred into the structure.

The oscillating current introduces a magnetic field that is strongest around the ring region. This field is confined near the surface of the antenna and lies in the plane of the substrate. All these reasons in this antenna design make it suitable for interacting with NV centres when a diamond sample is placed above the loop.

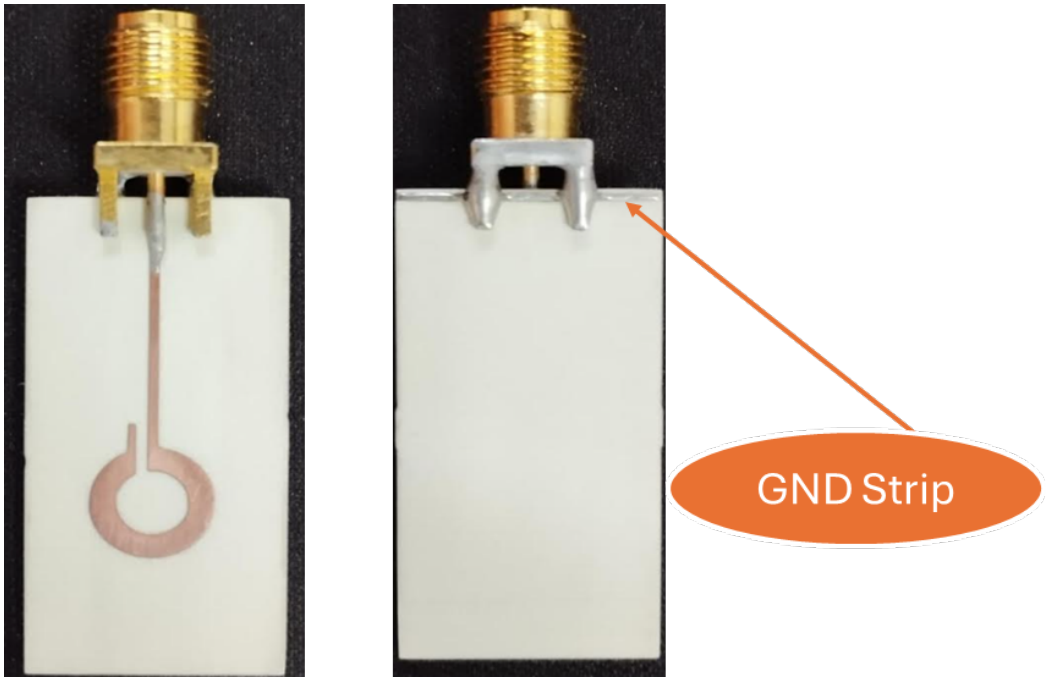


**Figure 3.6:** Fabricated annular loop antenna on the Rogers PCB

The tuning strip provides additional flexibility for the resonance. By slightly adjusting the tuning strip's length $L_1$, the resonance frequency can be shifted without changing the dimensions of the main loop. This tuning strip makes it useful in practice to compensate for fabrication variations or environmental effects.

### 3.4.3 Fabrication Using PCB Milling Process

This antenna design was fabricated using a PCB milling process, which allows rapid and clean prototyping without chemical etching.

The fabrication steps are as follows:

1. The antenna design was first designed in CAD software (FreeCAD and KiCAD), and then we export them as Gerber files.
2. These exported Gerber files were converted into milling toolpaths.
3. Used a precise milling bit to design the feedline, gap, and structure of the loop.
4. The PCB board was fixed on the milling platform base, and multiple shallow passes were used to remove unwanted copper.
5. After completing the milling process, we have cleaned the fabricated antenna using isopropanol to remove extra particles of metal and other materials.
6. An SMA connector was soldered, as shown in the Figure 3.6, to the feedline and ground plane for RF input.

This approach is really faster than chemical etching and avoids the use of hazardous chemicals, but the availability of the PCB milling facility can be a concern. Overall, these benefits make it suitable for quick testing and making different types of designs.

### 3.4.4 Why This Design Is Useful

- **Compact structure:** This antenna occupies a small area while working for high frequencies.
- **Efficient coupling:** The gap-based microwave feeding provides an excellent impedance matching required for the RF transmission.
- **Simple tuning:** The tuning strip makes easy shifting and adjustment of the resonance frequency.
- **Ease of fabrication:** This design can be fabricated using standard PCB milling techniques, but if this facility of PCB milling is not available, then it will become a costly process. In that case, chemical etching is one of the most suitable processes.
- **Suitable for ODMR:** The magnetic field can be locally applied near the loop, which is a very good point for coupling to NV centres.

### 3.4.5 Summary

In summary, this microstrip annular circular loop antenna design offers a simple way to transmit the microwave fields for NV-application experiments. Its compact geometry, good impedance matching, and short way of fabrication make it a practical option for laboratory setups and compact device making.

# Chapter 4

# Antenna Transmission And Bandwidth

In this chaper of this thesis, we analyse the performance of the fabricated antenna designs using reflection coefficient ($S_{11}$) measurements. These measurements were done using a vector network analyser (VNA, image attached in Fig. A.6) in the frequency range of interest. The goal is to see how closely the fabricated designs match the simulated response and to understand the effect of design variations.

## 4.1 Microstrip Antenna: Comparison of Simulation and Fabrication

To evaluate the performance of the microstrip antenna, three different versions of the design were fabricated. In these designs, the ground plane geometry was slightly modified while keeping the feedline and overall layout almost the same. This allows us to understand how sensitive the antenna performance is to small design changes.

The measured reflection coefficient ($S_{11}$) of all three fabricated antennas is compared with the simulated result in Fig. 4.1. As shown in Fig. 4.1, the simulated antenna result shows a sharp and deep resonance near $\sim 2.9$ GHz, with a return loss of about $-26$ dB. This is very good impedance matching in the ideal(simulation) case.

In comparison, the fabricated antennas show a similar trend but with very significant differences. The resonance dips are broader and not as deep as the simulated result. This is expected in real experiments due to fabrication imperfections and additional losses in the system.

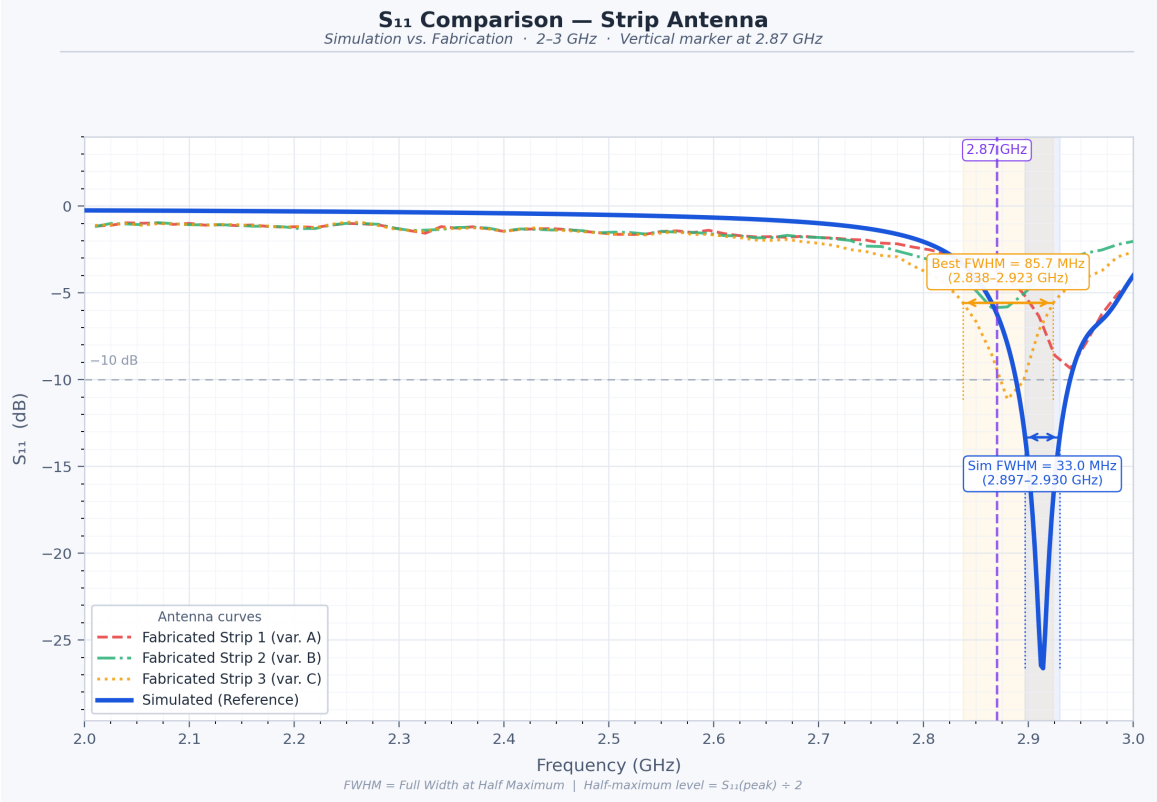


**Figure 4.1:** Comparison of simulated and fabricated strip antennas in the frequency range 2–3 GHz. The dashed horizontal line indicates the −10 dB level, and the shaded region highlights the bandwidth around the target frequency of 2.87 GHz.

A small shift in resonance frequency is also present there. The fabricated antennas resonate slightly away from the simulated value, which can be due to small errors in dimensions, variations in the FR-4 substrate properties, and the effect of soldering the SMA connector.

The geometrical differences between the simulated and fabricated strip antennas are summarised in Table 4.1. These variations are mainly introduced in the ground plane region to study their effect on antenna performance.

**All these dimensions are in millimetres**

### 4.1.1 Bandwidth Analysis

The bandwidth of the antenna is defined as the frequency range where $S_{11} < -10$ dB. This region is marked in Fig. 4.1.

The simulated microstrip antenna has a relatively narrow bandwidth of about $\sim 33$ MHz Fig. 4.1, indicating a sharp resonance. On the other hand, the fabricated antennas show a wider bandwidth. For example, Fabricated Strip 3 shows a bandwidth of approximately $\sim 85$ MHz, Fig. 4.1.

This difference in bandwidth comes with a trade-off. While the fabricated antennas cover a wider frequency range, the depth of the resonance is less; this thing shows

**Table 4.1:** Geometrical parameters of simulated and fabricated strip antennas

| **Parameter** | **Simulated** | **Strip 1** | **Strip 2** | **Strip 3** |
|---|---|---|---|---|
| *Substrate Dimensions* | | | | |
| $L$ | 26mm | 26mm | 26mm | 26mm |
| $W$ | 25mm | 25mm | 25mm | 25mm |
| *Ground Plane Variations* | | | | |
| $d$ (ground copper length) | 26mm | 24mm | 26mm | 23mm |
| $g$ (ground copper width) | 25mm | 23mm | 25mm | 23.5mm |
| *Feedline Geometry* | | | | |
| $W_1$ | 3mm | 3mm | 3mm | 2.5mm |
| $W_2$ | 5mm | 4.5mm | 5mm | 4.5mm |

that the impedance matching is not as strong as in the simulated design.

### 4.1.2 Comparison among different Fabricated Designs

The three fabricated antennas with a small change in parameters show clear differences in their performance, which shows that perfection in dimensions is very crucial (Fig. 4.1):

- **Fabricated Strip 1:** This antenna shows a moderate resonance with a depth less than the simulation, and a bit-shifted resonance indicates some mismatch.
- **Fabricated Strip 2:** Shows a slightly shifted resonance and a weaker dip, telling us high losses or variation in fabricated ground geometry.
- **Fabricated Strip 3:** It shows the best bandwidth and relatively better response among these all three fabricated designs, although the resonance is still shallower than the simulated case, but it is a considerable result.

These different designs confirm that the ground plane geometry/area can significantly affect the antenna behaviour.

### 4.1.3 Quantitative Comparison

In short, we can say that the key parameters that affect the performance, such as resonance frequency, minimum return loss, and bandwidth, are extracted from the measurements and listed in Table 4.2.

The differences between simulated and fabricated results can be dependent on some practical factors that we can see by watching the results of the different fabricated antennas within the same design, by changing the parameters a bit.

**Table 4.2:** Comprehensive comparison of simulated and fabricated strip antenna performance

| **Antenna** | $f_r$ **(GHz)** | $S_{11}$ **(dB)** | **Half-max(dB)** | **FWHM(GHz)** |
|---|---|---|---|---|
| Simulated | 2.914 | −26.63 | −13.31 | 2.897–2.930 |
| MicroStrip3 (Best fabricated) | 2.880 | −11.14 | −5.57 | 2.838–2.923 |

### 4.1.4 Near-field magnetic field distribution

To evaluate the spatial uniformity and strength of the microwave field generated by the microstrip antenna, a near-field scan was performed over the antenna aperture at the resonance frequency of 2.87 GHz. Figure 4.2 shows the simulation of the H-field distribution. The field is concentrated in the gap region, with a maximum of 18.312 A/m and a minimum of 0.451 A/m. Over the central area where the diamond sample is placed, the field variation is within ±15 %, indicating good spatial uniformity.

The peak H-field corresponds to a magnetic flux density $B = \mu_0 H \approx 23\ \mu$T, which is more than sufficient to drive Rabi oscillations and obtain clear ODMR contrast. This result confirms that the antenna not only accepts power efficiently ($S_{11} = -11.14$ dB) but also converts it into a strong, usable magnetic field at the sample location.

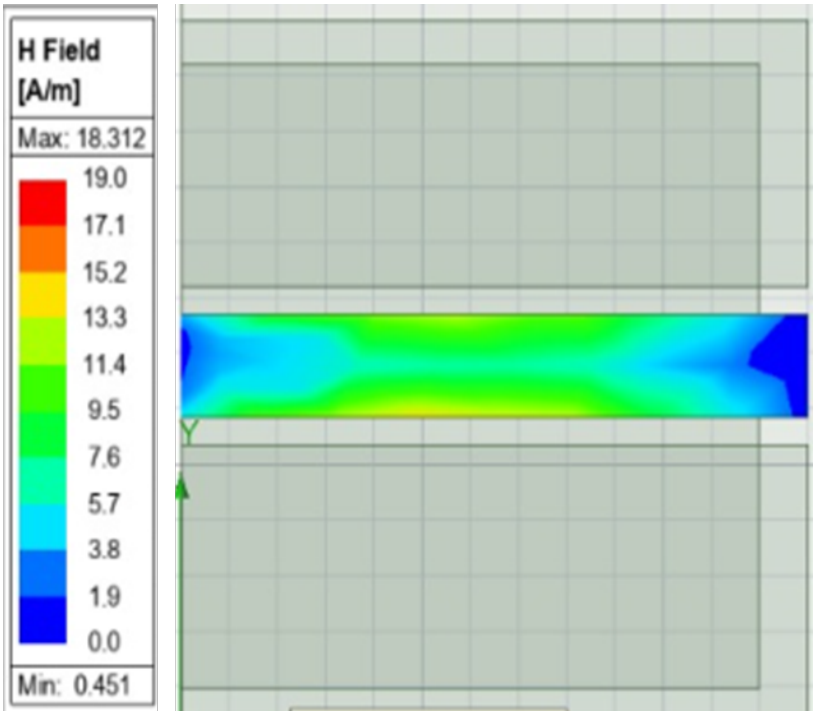


**Figure 4.2:** Near-field H-field distribution of the microstrip strip antenna at 2.87 GHz. The colour bar indicates the magnetic field strength in A/m. The maximum is 18.312 A/m and the minimum is 0.451 A/m.

First, fabrication tolerances such as slight variations in trace width, gap dimensions, and ground plane edges can significantly affect impedance matching. Even if there are very small deviations that can also make a noticeable effect at microwave frequency range, and that can shift, can lead to a shift in resonance [16].

Second, the FR-4 substrate can introduce additional dielectric losses that are not fully captured in ideal simulations, as substrate thickness and permittivity also contribute to frequency shifts. Also, the copper can get oxidised in the environment, which can make small Variations.

Third, the SMA connector and soldering can introduce some parasitic effects, which can alter the effective input impedance of the antenna.

Finally, the variation in ground plane geometry among the three fabricated designs directly impacts the current distribution and electromagnetic field confinement, leading to differences in the observed $S_{11}$ response.

Overall, the experimental results follow the same trend as the simulation, confirming the validity of the design. However, they also highlight the importance of careful fabrication and layout optimisation for achieving optimal performance.

## 4.2 Performance Analysis of Rectangular Loop Antenna

### 4.2.1 Comparison of Simulation and Fabrication

To further explore some other antenna designs for better performance and efficient microwave delivery, we fabricated a rectangular loop-based coplanar design [20]. Similar to the microstrip antenna, we fabricated three versions of this design to assess the effects of geometric variations on antenna performance [4].

The reflection coefficient ($S_{11}$) of the simulated and fabricated rectangular loop antennas is shown in Fig. 4.3 over the frequency range of 2–3 GHz. The simulated antenna exhibits a well-defined resonance near the target NV centre frequency of approximately 2.87 GHz. The resonance depth is sharp and very good, indicating strong impedance matching under ideal conditions.

The fabricated loop antennas show a bit different behaviour. While the overall trend follows the simulated response, the resonance dips are significantly broader and shallower. None of the fabricated antennas with small variations reaches the same depth as the simulated case. This difference indicates increased mismatch and high additional losses in the practical implementation.

Overall, in the three fabricated variants, Fabricated Loop 3 (variation C) shows the most significantly matching resonance behaviour 4.3. It achieves a better, wider

response around the target frequency, although the minimum $S_{11}$ value is still higher (less negative) compared to the simulation. Fabricated Loop 1 and Loop 2 give weaker resonance characteristics. These comparisons show that the specific geometric variations in those designs are less effective in achieving optimal impedance matching [].

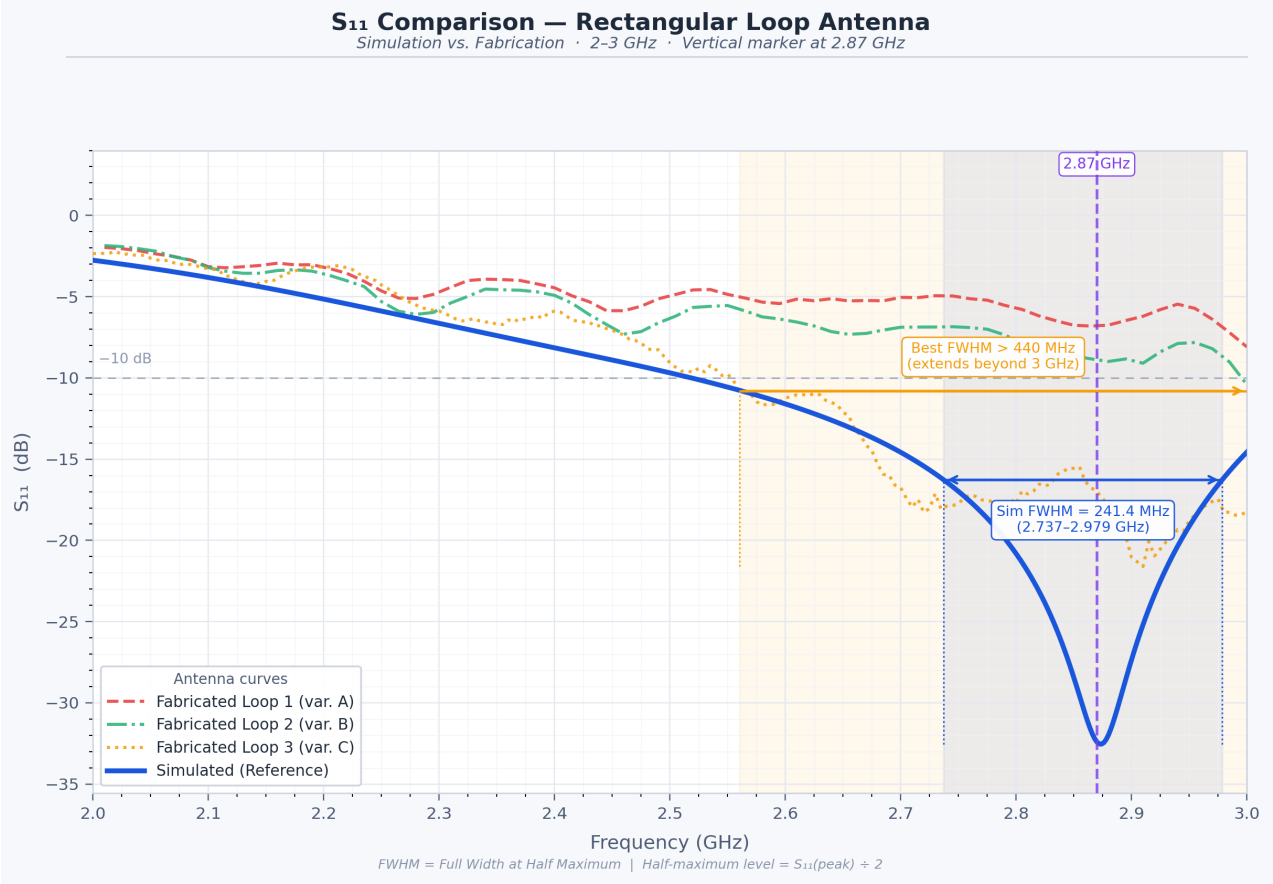


**Figure 4.3:** Comparison of simulated and fabricated rectangular loop antennas in the 2–3 GHz frequency range. The simulated design shows a sharp resonance near the target NV centre frequency (2.87 GHz), while the fabricated variants exhibit broader and shallower responses due to practical losses. The dashed horizontal line indicates the −10 dB threshold, and the shaded region highlights the bandwidth around the resonance.

In addition to the reflection coefficient measurement, the near-field H-field distribution of the rectangular loop antenna was characterised. Figure 4.4 summarises the measured field strengths over the antenna aperture at 2.87 GHz. The maximum H-field reaches 97.057 A/m, while the minimum is only 0.009 A/m. This large variation indicates that the field is highly concentrated in a small region near the loop gap, which is advantageous for localised excitation of NV centres. However, the wide range also suggests that precise sample placement is critical for achieving optimal spin driving.

The peak H-field corresponds to $B = \mu_0 H \approx 122\ \mu$T, which is exceptionally strong and more than adequate for NV spin manipulation. These results, together

with the $S_{11}$ data in Fig. 4.3, demonstrate that the rectangular loop antenna provides excellent field strength, albeit with a highly non-uniform distribution – a trade-off that is acceptable for many ensemble NV experiments where the diamond is placed directly in the high-field region.

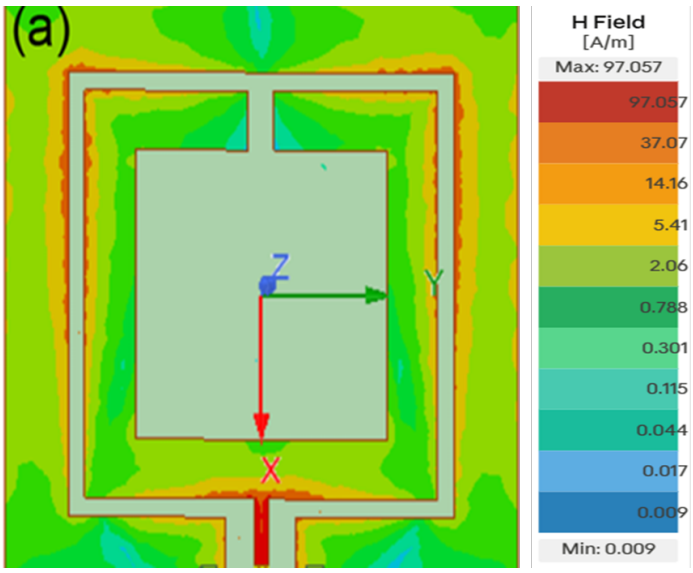


**Figure 4.4:** Near-field H-field statistics of the rectangular loop antenna at 2.87 GHz. The maximum field strength is 97.057 A/m, and the minimum is 0.009 A/m. (Image from the simulation.)

### 4.2.2 Bandwidth Analysis

The bandwidth of the antenna is defined as the frequency range over which $S_{11} \leq -10$ dB. This threshold is marked in Fig. 4.3 to clearly indicate the usable operating region of the antenna.

The simulated rectangular loop antenna shows a relatively confined bandwidth around the resonance region. However, the fabricated antennas display a broader response, particularly in the case of Fabricated Loop 3. The measured bandwidth for this design extends beyond 400 MHz, with the right edge exceeding the 3 GHz measurement limit. This indicates a significantly wider operational range compared to the simulated design.

While a larger bandwidth can be advantageous for NV applications, specifically, we need this large bandwidth for building the NV centre-based magnetometer. The broader response observed in the fabricated antennas is accompanied by a reduced depth of resonance, implying weaker impedance matching. This behaviour is consistent with increased losses and non-idealities in the fabricated system.

### 4.2.3 Comparison Between Fabricated Designs

The performance of the three fabricated loop antennas shows clear distinctions:

- **Fabricated Loop 1 (Variation A):** This antenna shows a weak resonance with a very small dip, telling us that there is poor impedance matching. The response remains relatively flat across the frequency range.
- **Fabricated Loop 2 (Variation B):** Shows a slightly better response compared to Loop 1, but still lacks a strong resonance feature near the target frequency.
- **Fabricated Loop 3 (Variation C):** Demonstrates the most favourable performance among the fabricated designs for our purpose. It shows a good bandwidth and a clearer resonance trend near the NV centre frequency, although the transmission is still not as deep as in the simulation.

All these observations suggest that even small geometric variations in the loop structure and ground configuration can significantly influence the current distribution and impedance characteristics of the antenna.

### 4.2.4 Quantitative Comparison

To further analyse the antenna performance, key parameters such as resonance frequency ($f_r$), the return loss ($S_{11}$), and bandwidth are understood and seen from the measurements and summarised in Table 4.3.

The simulated rectangular loop antenna shows a very clear resonance at 2.874 GHz with a very low return loss of $-32.54$ dB, which directly confirms our excellent impedance matching. In contrast, the best-performing fabricated design (Loop 3) shows a resonance dip at 2.910 GHz, corresponding to a frequency shift of approximately 36 MHz.

A degradation in return loss is also observed. The minimum $S_{11}$ parameter value increases from $-32.54$ dB in simulation to $-21.61$ dB in the fabricated case, describing the increased mismatch and additional losses in the practical implementation.

The bandwidth behaviour shows a clear trade-off. The simulated antenna exhibits a full width at half maximum (FWHM) of 241.4 MHz (2.737–2.979 GHz), whereas the fabricated Loop 3 shows a significantly broader FWHM, which exceeds 350 MHz. The right edge of the bandwidth extends beyond the 3 GHz measurement limit, so it provides an even wider operational range. That is a very good thing to drive the NV-centres transitions and for the NV-magnetometry.

For this good, large bandwidth, the resonance depth is compensated in this design. It is also consistent with the general trade-off between bandwidth and impedance

matching. The broader response in the fabricated antenna can be attributed to increased losses and reduced quality factor (Q-factor).

The observed differences between simulation and experiment arise from several practical factors. Fabrication tolerances, including variations in trace width and spacing, can alter the effective electrical length of the antenna. The FR-4 substrate introduces dielectric losses (loss tangent) that are not fully captured in ideal simulations. Additionally, parasitic capacitance and inductance introduced by the SMA connector and soldering further affect the impedance characteristics.

Overall, the fabricated rectangular loop antenna follows the general trend predicted by simulation but exhibits broader bandwidth and reduced matching efficiency. Among the tested designs, Loop 3 provides the best compromise between bandwidth and resonance behaviour near the NV centre frequency.

**Table 4.3:** Quantitative comparison of simulated and fabricated rectangular loop antenna performance

| **Antenna** | $f_r$ **(GHz)** | $S_{11}$**(dB)** | **Half-max(dB)** | **FWHM(GHz)** |
|---|---|---|---|---|
| Simulated | 2.874 | $-32.54$ | $-16.27$ | 2.737 – 2.979 |
| Loop 3 (best fabricated) | 2.910 | $-21.61$ | $-10.80$ | $> 0.350$ (extends beyond 3 GHz) |

# Chapter 5

# Conclusion and Future Work

## 5.1 Conclusion

In this work, we have explored the design, fabrication, and characterisation of microwave antennas for driving spin transitions in NV-centre-based systems. The primary objective was to develop simple, low-cost, and efficient antenna structures that can deliver microwave fields efficiently near the NV resonance frequency of 2.87 GHz.

We began by understanding the physical requirements of NV-centre spin manipulation, particularly the need for efficient impedance matching, sufficient bandwidth, and a considerable uniform microwave magnetic fields around the sample region. Based on these requirements, multiple PCB-based antenna geometries were designed and fabricated using accessible techniques such as ferric-chloride etching and PCB milling.

Two main classes of antenna designs were investigated in detail: microstrip-based structures and coplanar rectangular loop antennas. The simulated and experimentally measured $S_{11}$ responses show that while simulations give sharp and deep resonances. But the fabricated antennas exhibit broader and shallower responses due to practical factors such as fabrication tolerances, dielectric losses in FR-4, and some other effects from connectors and soldering.

Despite these deviations, the fabricated antennas demonstrate good performance near the target frequency. The optimised loop-based design achieves a bandwidth of more than 300 MHz around 2.87 GHz, which is very good for ODMR experiments where frequency shifts occur due to external magnetic fields. The results confirm that simple PCB-based antennas can effectively deliver microwave power for NV-centre applications without requiring complex or expensive fabrication methods.

Overall, this work establishes a complete workflow—from design and simulation to fabrication and experimental validation—for developing microwave delivery systems tailored to NV-based quantum sensing [13].

## 5.2 Future Work

While the present work focuses on antenna design and characterisation, the next step is to integrate these components into a complete ODMR-based magnetic field sensing system [22].

The primary goal of future work is to develop a **low-cost, compact, and hands-on NV-based magnetometer** using the optimised antenna designs presented in this thesis. The idea is to build a miniaturised experimental setup that can demonstrate ODMR measurements in a simple and accessible manner, making it suitable for laboratory training, educational purposes, and portable sensing applications [22].

A key advantage of this approach is that most of the required components are already available in low-cost and compact form. In particular, RF signal generation and amplification can be achieved using affordable modules, which have been detailed in the Appendix. Although we need a very optimised performing antenna for these RF transmissions, in an optimised and very good transmission case, these compact RF generators(ADF4351) A.3 and a small RF amplifier, as shown in Fig. A.3, are sufficient for driving the NV spin transitions.

The optimised antenna developed in this work will play a central role in this setup by ensuring efficient microwave delivery to the diamond sample [23]. Combined with a simple optical detection system (photodiode or camera-based), this will enable the observation of ODMR signals without the need for highly specialised equipment.

In addition to building the complete system, several improvements can be explored:

- Further optimisation of antenna geometry to improve field uniformity across the sample.
- Exploration of alternative substrate materials with lower dielectric loss compared to FR-4.
- Integration of the antenna and sample holder into a single compact module.
- Extension to pulsed ODMR techniques, including Rabi oscillations and Ramsey spectroscopy.

In the long term, this work can contribute towards the development of portable and scalable quantum sensing devices based on NV centres. By combining low-cost hardware with optimised antenna design, it becomes possible to move towards practical and widely accessible quantum technologies.

# Bibliography


[1] H. Babashah, H. Shirzad, E. Losero, V. Goblot, C. Galland, and M. Chipaux, SciPost Physics Core **6**, 065 (2023).

[2] J. Herrmann, M. A. Appleton, K. Sasaki, Y. Monnai, T. Teraji, K. M. Itoh, and E. Abe, Applied Physics Letters **109**, 183111 (2016).

[3] K. Sasaki, Y. Monnai, S. Saijo, R. Fujita, H. Watanabe, J. Ishi-Hayase, K. M. Itoh, and E. Abe, Review of Scientific Instruments **87**, 053904 (2016).

[4] L. Rondin, J.-P. Tetienne, T. Hingant, J.-F. Roch, P. Maletinsky, and V. Jacques, Reports on Progress in Physics (2014).

[5] M. W. Doherty, N. B. Manson, P. Delaney, F. Jelezko, J. Wrachtrup, and L. C. L. Hollenberg, Physics Reports (2013).

[6] C. Teale, *Magnetometry with NV Ensembles*, Master's thesis, MIT (2015).

[7] L. Troise, *Biomagnetic Sensing with NV Centers*, Ph.D. thesis, Technical University of Denmark (2021).

[8] P. Neumann, *Quantum Information Processing with NV Centers*, Ph.D. thesis, University of Stuttgart (2012).

[9] D. Misonou, K. Sasaki, S. Ishizu, Y. Monnai, K. M. Itoh, and E. Abe, AIP Advances **10**, 025206 (2020).

[10] O. R. Opaluch, N. Oshnik, R. Nelz, and E. Neu, Nanomaterials **11**, 2108 (2021).

[11] H. Zhang, C. Belvin, W. Li, J. Wang, J. Wainwright, R. Berg, and J. Bridger, American Journal of Physics **86**, 225 (2018).

[12] S. V. Titkov, V. V. Yakovleva, I. D. Breev, R. A. Babunts, P. G. Baranov, and N. S. Bortnikov, Diamond and Related Materials **136**, 109938 (2023).

[13] Y. Chen, T. Li, G. Chai, D. Wang, B. Lu, A. Guo, and J. Tian, Nanomaterials **12**, 3938 (2022).

[14] C. A. Balanis, Wiley (2016).

[15] D. M. Pozar, Wiley (2012).

[16] L.-L. Yang, G.-Q. Liu, X.-Y. Pan, and D.-M. Chen, Chinese Physics Letters **27**, 038401 (2010).

[17] R. P. Jedlicka, M. T. Poe, and K. R. Carver, IEEE Transactions on Antennas and Propagation (1981).

[18] H. A. Wheeler, IEEE Transactions on Microwave Theory and Techniques (1965).

[19] W. Jia, Z. Shi, X. Qin, X. Rong, and J. Du, Review of Scientific Instruments **89**, 064705 (2018).

[20] S. Mahtab, P. Milas, D.-T. Veal, M. G. Spencer, and B. Ozturk, Review of Scientific Instruments **94**, 044701 (2023).

[21] M. Zhao, Q. Lin, L. Zhu, L. Zhao, and Z. Jiang, Micro & Nano Letters (2020).

[22] J. Stegemann, M. Peters, L. Horsthemke, N. Langels, P. Glosekotter, S. Heusler, and M. Gregor, European Journal of Physics **44**, 035402 (2023).

[23] A. Bulau, D. Walter, and K.-P. Fritz, Magnetism **5**, 18 (2025).

# Appendix A

# Experimental Setups and other Essential Components

## A.1 PL- Detection Setup and spectrum

Here in figure A.1, I am attaching the original setup that we were using for seeing the spectrum and the photoluminescence from the diamond sample.

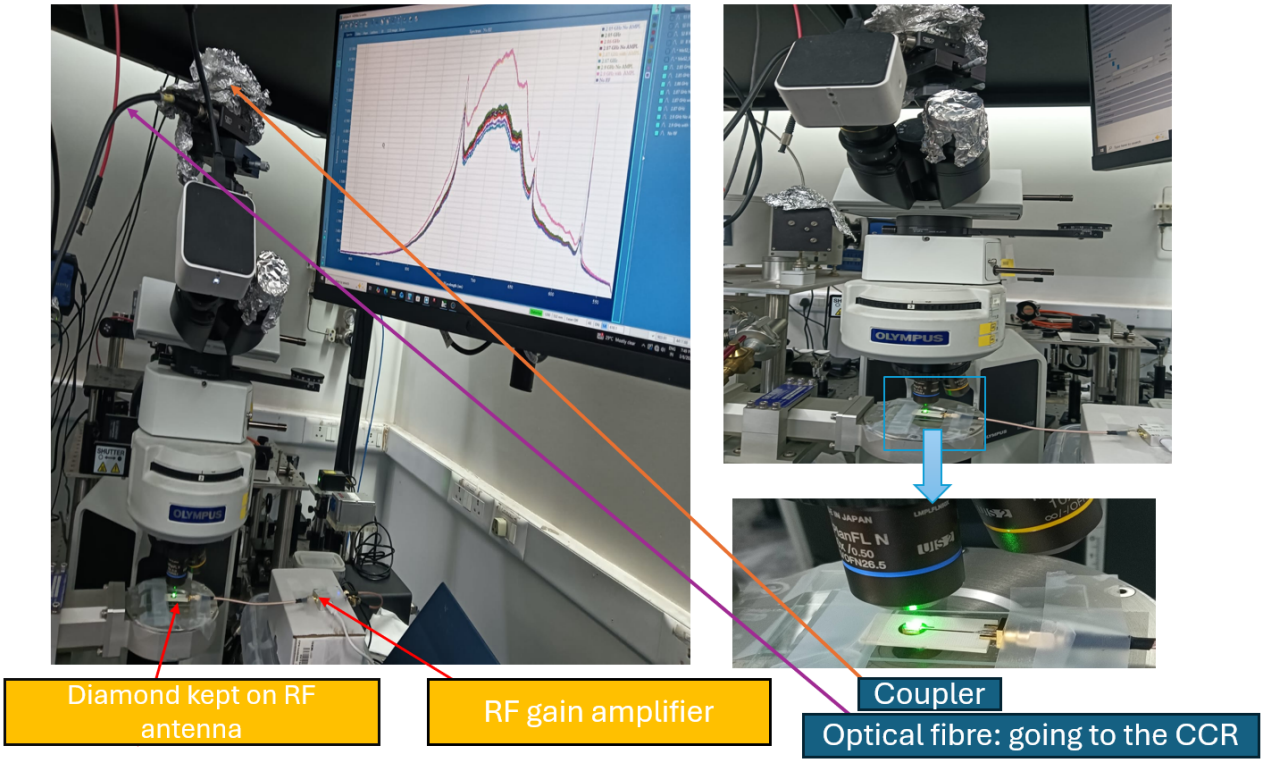


**Figure A.1:** The complete setup used for the PL-detection in this experiment

## A.2 Real Time PL-Spectrum

Here I am attaching the real-time spectrum for the photoluminescence directly collected by the CCD Camera present in the setup described in the Figure A.2.

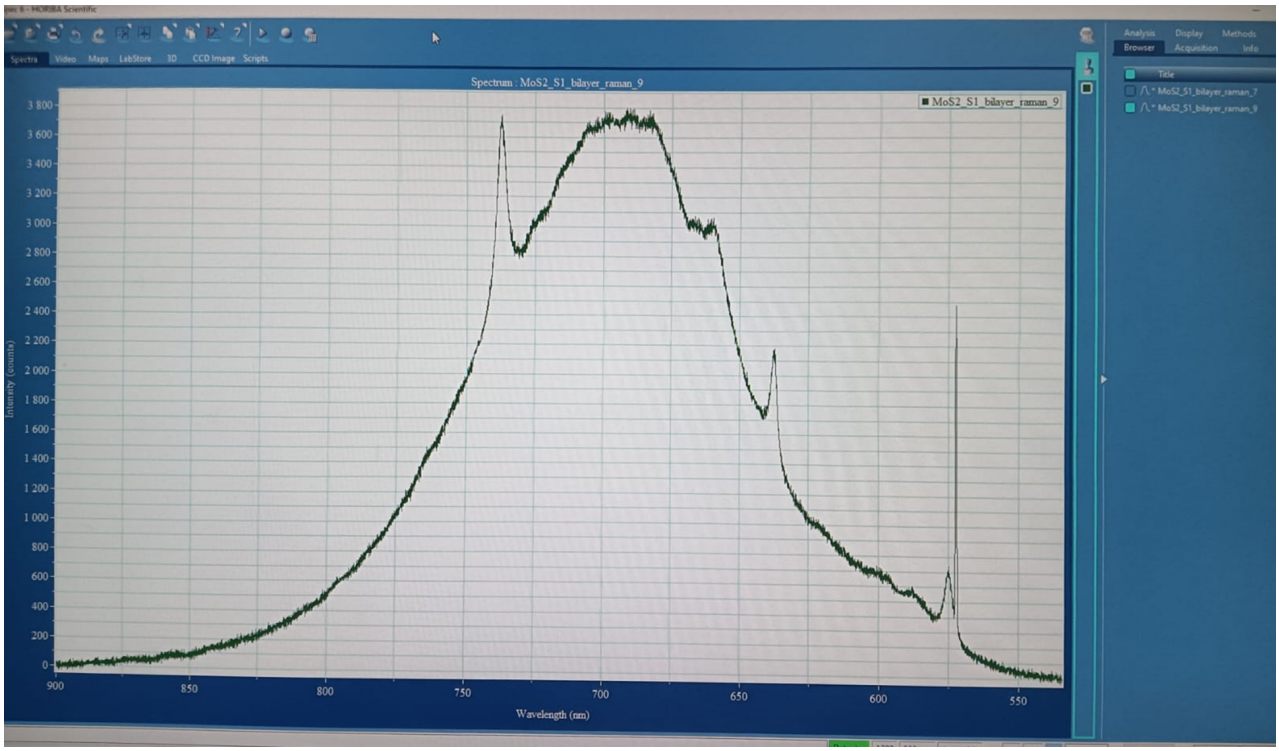


**Figure A.2:** Real-time PL collected at CCD Camera

## A.3 Main RF Components

Here in this section, I have described the key RF components used for microwave generation and amplification in the experimental setup. The primary objective was to develop a compact and cost-effective system capable of delivering microwave signals near the NV centre resonance frequency ( 2.87 GHz) for ODMR measurements.

The RF generation includes two main elements: a compact RF signal generator and a broadband RF amplifier. The RF generator provides a tunable microwave signal at the needed frequency range, while the amplifier boosts the signal power to make efficient delivery to the antenna [22].

Figure A.3 shows the complete hardware used in the setup. Panel (a) illustrates the RF signal generator module, which is controlled electronically and allows frequency tuning over a wide range. Panel (b) shows the RF gain amplifier, designed to operate in the GHz range and provide sufficient power amplification. Panel (c) presents the complete connection setup, where the RF generator output is fed into the amplifier

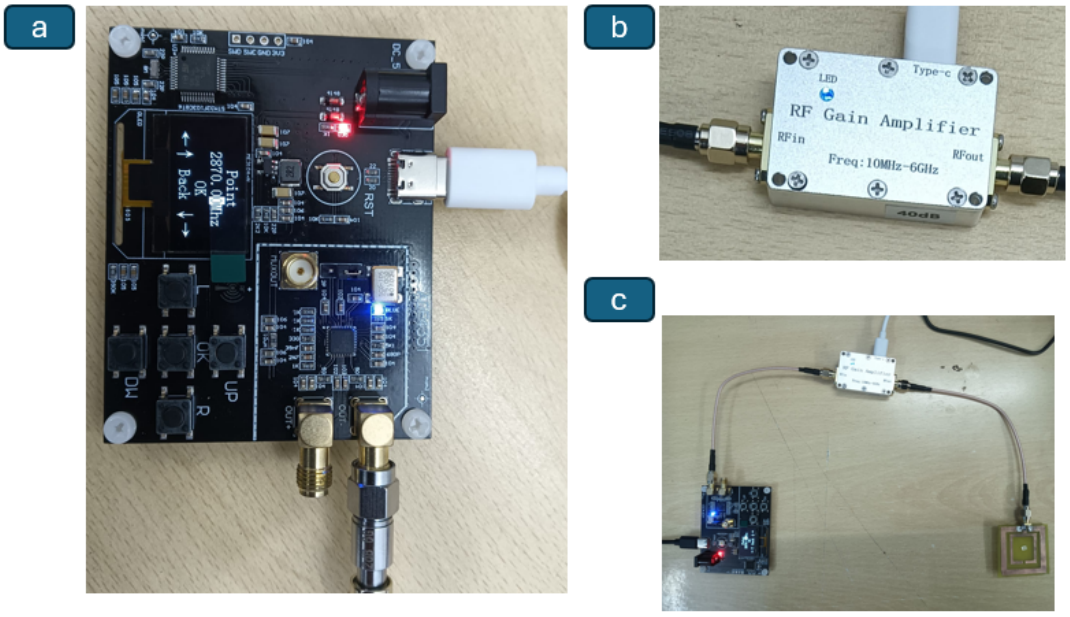


**Figure A.3:** Main RF components used in the experimental setup: (a) compact RF signal generator module(ADF4351), (b) RF gain amplifier operating in the GHz range, and (c) complete connection setup showing signal flow from generator to amplifier and antenna.

and then delivered to the fabricated antenna via coaxial cables.

These compact and low-cost components make the system accessible and suitable for building a portable ODMR setup without relying on expensive laboratory-grade microwave sources. These modules provide adequate performance for driving NV spin transitions and acquiring ODMR signals along with the benefit of their simplicity.

## A.4 Overview of the Complete Experimental Setup for ODMR

Figure A.5 shows the full experimental setup used in this work to probe ODMR in the NV-centre diamond sample. The setup brings together optical excitation, microwave delivery, and signal detection in a single arrangement [9].

At the heart of the setup is an optical microscope. It is used to focus the laser light onto the diamond and also to collect the emitted fluorescence. A green laser (around 532 nm) is used to excite the NV centres and initialise them into the $m_s = 0$ state. When the NV centres are driven, they emit fluorescence, which is collected through the same optical path and sent to a detector or imaging system.

For microwave excitation, we use an RF chain consisting of a signal generator followed by an RF amplifier. This signal is delivered to the fabricated antenna placed

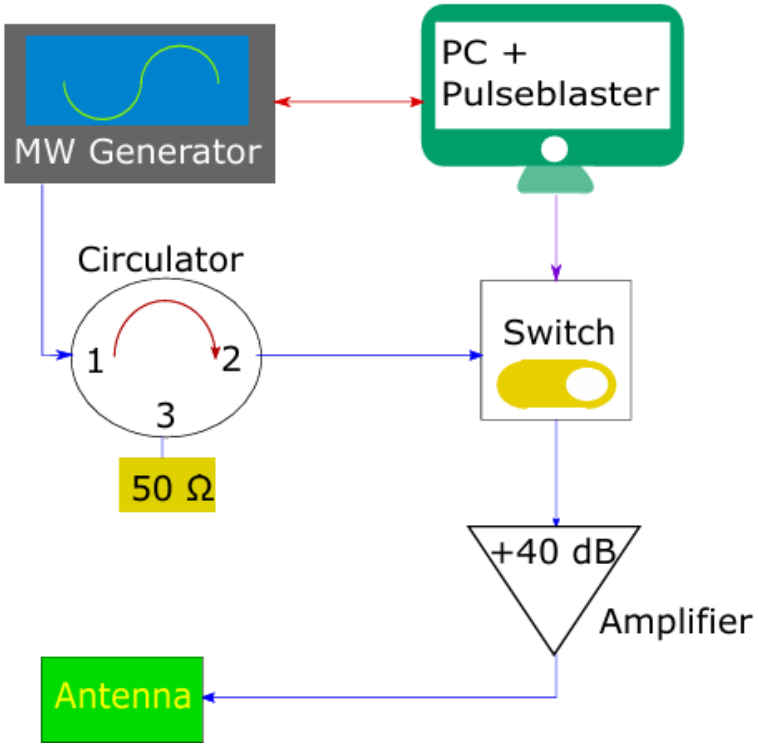


**Figure A.4:** All components used in the Microwave circuit for RF transmission

close to the diamond. The idea is to generate a sufficiently strong microwave magnetic field to drive the spin transitions of the NV centres.

In addition to these main components, the setup also includes positioning stages to carefully align the sample, along with electronic instruments for controlling the signals. A computer interface is used to monitor the measurements and record the data.

At the present stage, a clear ODMR signal has not yet been observed. This could be due to several reasons — alignment issues, insufficient microwave power, or losses in the optical collection. Background noise may also be an error. That said, the setup itself is complete and functional. With further optimisation, especially in alignment and antenna performance, we expect to observe a reliable ODMR signal.

## A.5 How to use VNA

A Vector Network Analyser (VNA) is one of the most important instruments used in this work for characterising the microwave performance of fabricated antennas. It allows us to measure how efficiently the antenna transmits and reflects microwave signals at a particular frequency. This instrument model also allowed us to watch the

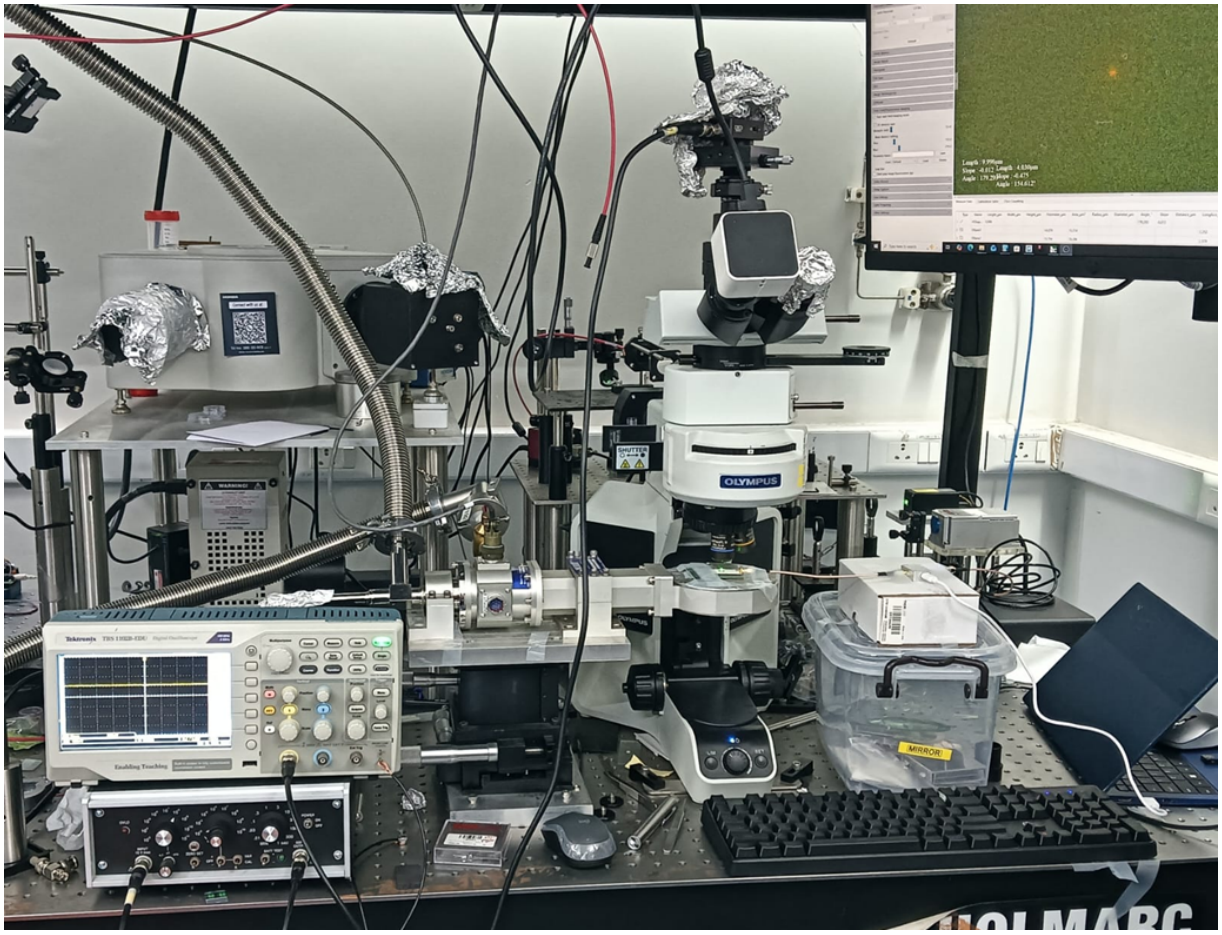


**Figure A.5:** Experimental setup for ODMR measurements, showing the optical microscope system, RF circuit for microwave delivery, and associated electronic instrumentation.

spectrum of RF generators in the required range.

The basic idea for using a VNA is to send a known microwave signal into the antenna and analyse how much of that signal is reflected back. This is quantified using the reflection coefficient ($S_{11}$), which gives direct information about impedance matching and resonance behaviour. A lower value of $S_{11}$ (typically below $-10$ dB) indicates that most of the input power is successfully delivered to the antenna.

To perform a measurement, the antenna is first connected to the VNA using a coaxial cable through an SMA connector. Before taking data, calibration of the VNA is essential to remove systematic errors due to cables and connectors.

Once calibration is done, the frequency range of interest (typically around 2–3 GHz for NV-centre applications) is selected. The VNA then sweeps across this frequency range while recording the reflection response. The resulting plot of $S_{11}$ versus frequency allows us to identify the resonance frequency, bandwidth, and overall performance of the antenna.

In the instrument shown in Fig. A.6, different ports are used depending on the measurement type. The vector analyser port is used for measuring parameters such

as $S_{11}$, while the RF input port can be used for spectrum analysis in the RF generator source.

Using this method, we can systematically compare different antenna designs and optimise their performance for efficient microwave delivery in ODMR experiments.

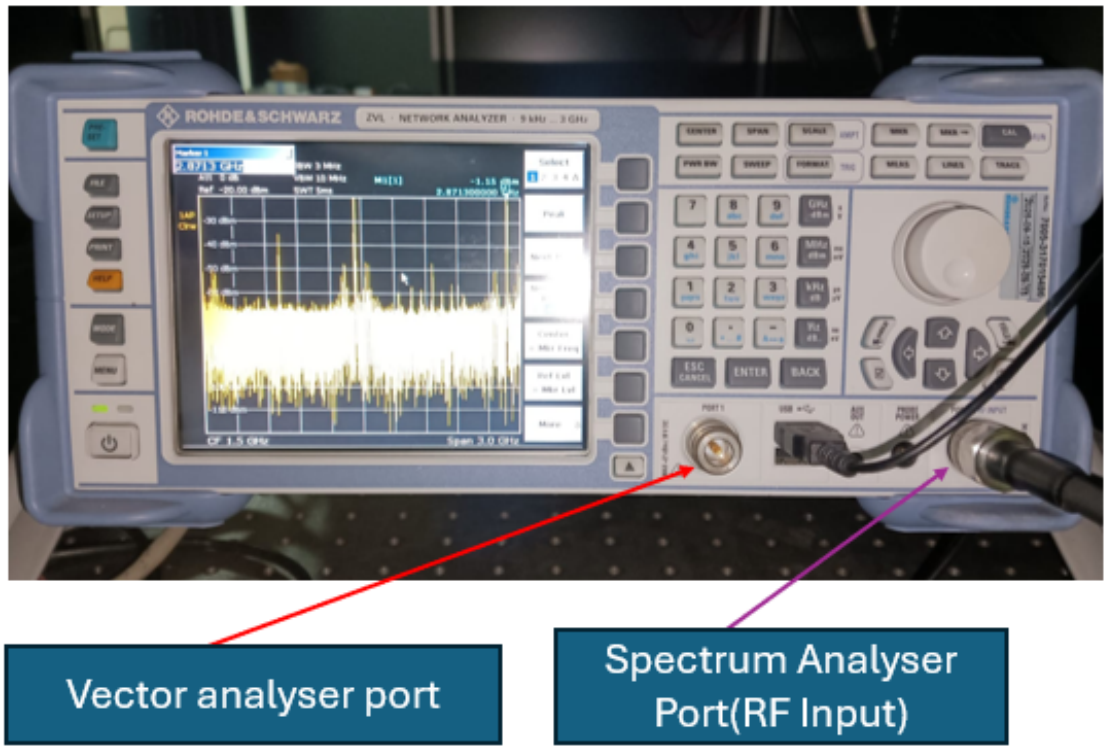


**Figure A.6:** VNA instrument Interface